SECS Analysis of Nighttime Magnetic Perturbation Events Observed in Arctic Canada

James M. Weygand[1], Mark J. Engebretson[2], Viacheslav A. Pilipenko[2,3], Erik S. Steinmetz[2], Mark B. Moldwin[4], Martin G. Connors[5], Yukitoshi Nishimura[6], Larry R. Lyons[7], and Christopher T. Russell[1], Shin Ohtani[8], and Jesper Gjerloev[8]

[1] Department of Earth Planetary and Space Sciences, University of California, Los Angeles, CA
[2] Department of Physics, Augsburg University, Minneapolis, MN
[3] Space Research Institute, Moscow, Russia
[4] Department of Climate and Space Sciences and Engineering, University of Michigan, Ann Arbor, MI
[5] Athabasca University, Athabasca, AB, Canada

[6] Department of Electrical and Computer Engineering and Center for Space Physics, Boston University, Boston, MA, USA
[7] Department of Atmospheric and Oceanic Sciences, University of California, Los Angeles, CA
[8] Johns Hopkins University Applied Physics Laboratory, Laurel, MD

submitted to the *Journal of Geophysical Research: Space Physics*

17 September 2021

Abstract

Large changes of the magnetic field associated with magnetic perturbation events (MPEs) with amplitudes |Δ*B*| of hundreds of nT and 5–10 min duration have been frequently observed within a few hours of midnight. This study compares the statistical location of nighttime MPEs with |d*B*/d*t*| ≥ 6 nT/s within the auroral current system observed during 2015 and 2017 at two stations, Cape Dorset and Kuujjuarapik, in Eastern Canada. Maps of the two dimensional nightside auroral current system were derived using the Spherical Elementary Current Systems (SECS) technique. Analyses were produced at each station for all events, and for premidnight and postmidnight subsets. We examine four MPE intervals in detail, two accompanied by auroral images, and show the varying associations between MPEs and overhead ionospheric current systems including electrojets and the field-aligned like currents. We find 225 of 279 MPEs occurred within the westward electrojet and only 3 within the eastward electrojet. For the premidnight MPEs 100 of 230 events occurred within the Harang current system while many of the remainder occurred within either the downward region 1 current system or the upward region 2 current system. Many of the 49 postmidnight MPEs occurred in either the downward region 1 (11 events) or upward region 2 current system (27 events). These result suggest that the source of MPEs in the premidnight sector is somewhere between the inner to mid plasma sheet and the source for the MPEs in the postmidnight sector is somewhere between the inner magnetosphere and the inner plasma sheet.

1. Introduction

Magnetic perturbation events (MPEs) are large rapid changes in the magnetic field with amplitudes |ΔB| of hundreds of nT, which can appear in any component, and with durations of about 5-10 min. MPEs are of interest because they can induce geomagnetically-induced currents (GICs) that can harm technological systems. Over the last several years a series of studies has investigated the properties and possible mechanisms that produce MPEs (Viljanen and Tanskanen, 2011; Engebretson et al., 2019a; b; 2020; 2021a; 2021b). To date, however, a detailed understanding of the chain of physical processes that produce MPEs is still not yet known, and accurate predictions of their occurrence cannot yet be made.

Viljanen and Tanskanen (2011) and Engebretson et al. (2019a;b) have noted that extreme MPEs often occur at typical auroral latitudes between 60° and 75° MLat and are limited in their spatial extent (radius ~ 275 km). Engebretson et al. (2019a; b) began a survey of ≥ 6 nT/s MPEs observed at high latitude stations during 2015 and 2017 in eastern Arctic Canada, part of four different magnetometer arrays. They presented statistical results using data from these arrays, and presented three case studies using auroral imagers and spacecraft data as well. In Engebretson et al. (2021a), as well as another study that compared MPEs observed in the Arctic and Antarctic using additional stations in Greenland (Engebretson et al., 2020), that showed several differences in characteristics between premidnight and postmidnight MPEs. These studies showed some of the postmidnight events were associated with auroral omega bands, which had been previously observed by Viljanen et al. (2001) and Apatenkov et al. (2020). Both the postmidnight intervals reported by Engebretson et al. (2020) and by Apatenkov et al. (2020) and Chinkin et al., (2021) consisted of a quasi-periodic series of MPEs with varying amplitudes. In the most recent study on MPEs Engebretson et al. (2021b) presented a superposed epoch analysis of these MPEs as functions of the interplanetary magnetic field, the dynamic pressure, density and velocity of the solar wind, and the SML, SMU, and SYM/H magnetic activity indices. Analysis plots were produced separately at each station for premidnight and postmidnight MPEs, and for three ranges of time after the most recent substorm onset: A) 0-30 min, B) 30-60 min, and C) >60 min. This study showed that the interplanetary magnetic field was typically negative prior to the MPE for the three ranges of time after the most recent substorm onset but no clear correlation with the solar wind plasma or SYM-H was identified. The SuperMAG auroral SML index showed a decrease and the SMU index displayed an increase during the 0-30 min and 30-60 min time ranges after the most recent substorm.

In this study we build on the database of large nighttime MPEs from Engebretson et al. (2021a;b) and provide complementary information on ionospheric currents during these events using the spherical elementary current system (SECS) method in order to understand where MPEs occur within the nightside auroral current system during or after auroral substorms. The SECS technique produces empirical summaries of the horizontal equivalent currents and vertical current amplitudes (proxies for the field-aligned currents) in the ionosphere over a large region over North America and Greenland (Weygand et al., 2011).

Section 2 describes the data used in this study and the procedure used to identify and quantify MPEs, and section 3 describes the SECS technique. In section 4 of this study we present a statistical SECS analysis of all MPEs observed at two of the five stations. In addition, for four selected MPE intervals we present in section 5 empirical maps of the equivalent currents and current amplitudes in the ionosphere over a large region over North America and Greenland produced using the SECS technique and auroral images obtained by THEMIS all-sky white light imagers (Mende et al., 2008), and compare them to time series plots of ground magnetometer data, SML and SMU index data, and the Bz component of the IMF. Section 6 summarizes these observations and discusses their implications in the light of other recent studies, and section 7 presents our conclusions and remaining open questions.

2. Magnetometer Data Set and Prior Studies

This study builds on a database of all the MPEs with derivative amplitudes |dB/dt| ≥ 6 nT/s within any of the individual magnetic field components observed during 2015 and 2017 at five stations in Arctic Canada (Engebretson et al., 2021a,b). To obtain the derivative amplitudes the magnetic field for each component was numerically differentiated using the 3-point Lagrangian approximation, $dB/dt[i] = (B[i+1] - B[i-1]) / 2\Delta t$ (where Δt is the time step, 0.5 s for both Cape Dorset and Kuujjuarapik). A ten-point smoothing was applied to the magnetic field data before the numerical differentiation in order to remove the effects of instrumental jitter and to eliminate isolated bad data points. The 10-point smoothing reduced the amplitude of single-point errors to values below those of the derivatives of large perturbation events as well as reduced the peak values of derivatives by consistently much less than 5%. This procedure is the same as the one applied in Engebretson et al. [2019a]The five Arctic stations used are Repulse Bay and Cape Dorset, part of the MACCS array described in Engebretson et al. (1995) and have 0.5 s resolution data; Iqaluit part of the CANMOS array described in Nikitina et al. (2016) and has 1 s resolution data; and Salluit and Kuujjuarapik, part of the AUTUMNX array described in Connors et al. (2016) and have 0.5 s resolution data. For each event, this database included the magnitude and vector components of the interplanetary magnetic field (IMF), the solar wind pressure, number density, and speed, the SYM/H index, and the SuperMAG versions (SML and SMU) of two auroral activity indices (AL and AU). The locations of these stations as well as others included in this paper are shown in **Figure 1**, and **Table 1** lists their geographic and corrected geomagnetic coordinates and data sampling rates.

Figure 2 displays a histogram of the duration of the derivative amplitudes above 6 nT/s for both Cape Dorset and Kuujjuarapik during 2015. The bins are 5 s. The peak of the distribution of the durations of the derivative amplitudes |dB/dt| ≥ 6 nT/s, which are different from the duration of the MPEs, was between 10 and 15 s, but the range for each station was between a few seconds (most common for MPEs with peaks only slightly above 6 nT/s) up to 71 s.

Table 1. Locations of the magnetometer stations used in this study. Geographic and corrected geomagnetic (CGM) latitude and longitude are shown, as well as the universal time (UT) of local magnetic noon, and the data sampling rate. Note that the CGM coordinates were calculated for epoch 2015, using http://sdnet.thayer.dartmouth.edu/aacgm/aacgm_calc.php#AACGM.

Array	Station	Station Code	Geo. Lat.	Geo. Long.	CGM Lat.	CGM Long.	UT of Mag	Sampling Rate

							Noon	(Hz)
MACCS	Repulse Bay	RBY	66.5°	273.8°	75.2°	-12.8	17:47	2.0
MACCS	Cape Dorset	CDR	64.2°	283.4°	72.7°	3.0°	16:58	2.0
CANMOS	Iqaluit	IQA	63.8°	291.5°	71.4°	15.1°	16:19	1.0
CANMOS	Sanikiluaq	SNKQ	56.5°	280.8°	65.7°	-1.9°	17:13	1.0
AUTUMNX	Salluit	SALU	62.2°	284.3°	70.7°	4.1°	16:54	2.0
AUTUMNX	Puvurnituq	PUVR	60.1°	282.7°	68.8°	1.4°	17.21	2.0
AUTUMNX	Inukjuak	INUK	58.5°	281.9°	67.3°	0.0°	17:16	2.0
AUTUMNX	Kuujjuarapik	KJPK	55.3°	282.2°	64.7°	0.2°	17:06	2.0
AUTUMNX	Radisson	RADI	53.8°	282.4°	63.0°	0.4°	16:48	2.0

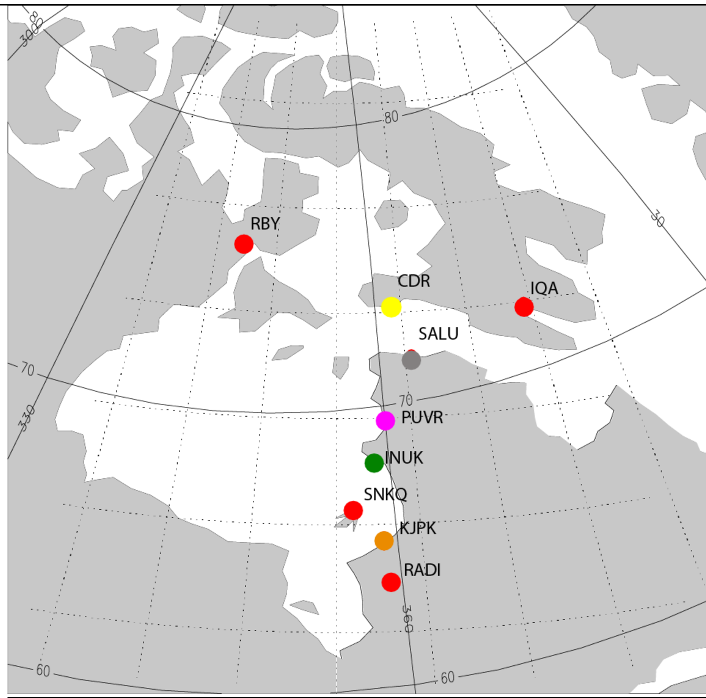

Figure 1. Map of ground magnetometer stations used for this study. Selected latitude and longitude lines in geomagnetic coordinates are shown. Some stations have been given specific colors because they will be discussed later: CDR (yellow), SALU (gray), PUVR (mauve), INUK (green), and KJPK (orange).

The companion paper (Engebretson et al., 2021b) builds on the database of large nighttime MPEs used in Engebretson et al. (2021a) to present a superposed epoch analysis of these MPEs as functions of the interplanetary magnetic field, the solar wind dynamic pressure, density, the velocity, the SML index, SMU index, and SYM/H index. Analysis plots in Engebretson et al. (2021b) were produced separately at each station for premidnight and postmidnight MPEs, and for three ranges of time after the most recent identified substorm onset: A) 0-30 min, B) 30-60 min, and C) >60 min. By providing detailed information on the temporal dependence of these events as functions of both external variables and geomagnetic activity indices, Engebretson et al. (2021b) provided statistical associations that may be helpful for understanding the physical mechanisms involved in their generation.

Engebretson et al. (2021b) showed that all of the ≥ 6 nT/s MPEs observed at these stations fell into the magnetic local time (MLT) range from 17 to 07 MLT. Two populations were evident in that study: a broad "premidnight" distribution extending from dusk to shortly after midnight (17 to 1 MLT) that appeared at all latitudes shown, and a "postmidnight" distribution from 2 to 7 MLT that was prominent only at the lower latitude stations. These MPEs were also divided into three categories based on the time of MPE occurrence after the closest prior substorm onset: $\Delta t_{so} \leq 30$ min, $30 < \Delta t_{so} < 60$ min, and $\Delta t_{so} \geq 60$ min. **Table 2** presents the numerical and percentage distributions of MPEs at CDR and KJPK in these six MLT and Δt_{so} categories that will be used further in section 4 of this study. In **Figure 2** we displayed a histogram of the duration of all MPEs. For each of these categories we examine the mean and error of the mean of the duration of the MPEs for each of the three substorm categories. We find the MPE duration during substorms to be longer than non-substorm MPEs. For $\Delta t_{so} \leq 30$ min category the mean duration is 19.0±0.9 s, for $30 < \Delta t_{so} < 60$ min the duration is 17.7±2.1 s, and for $\Delta t_{so} \geq 60$ min the mean duration is 12.8±1.8 s where the uncertainty given is the error of the mean.

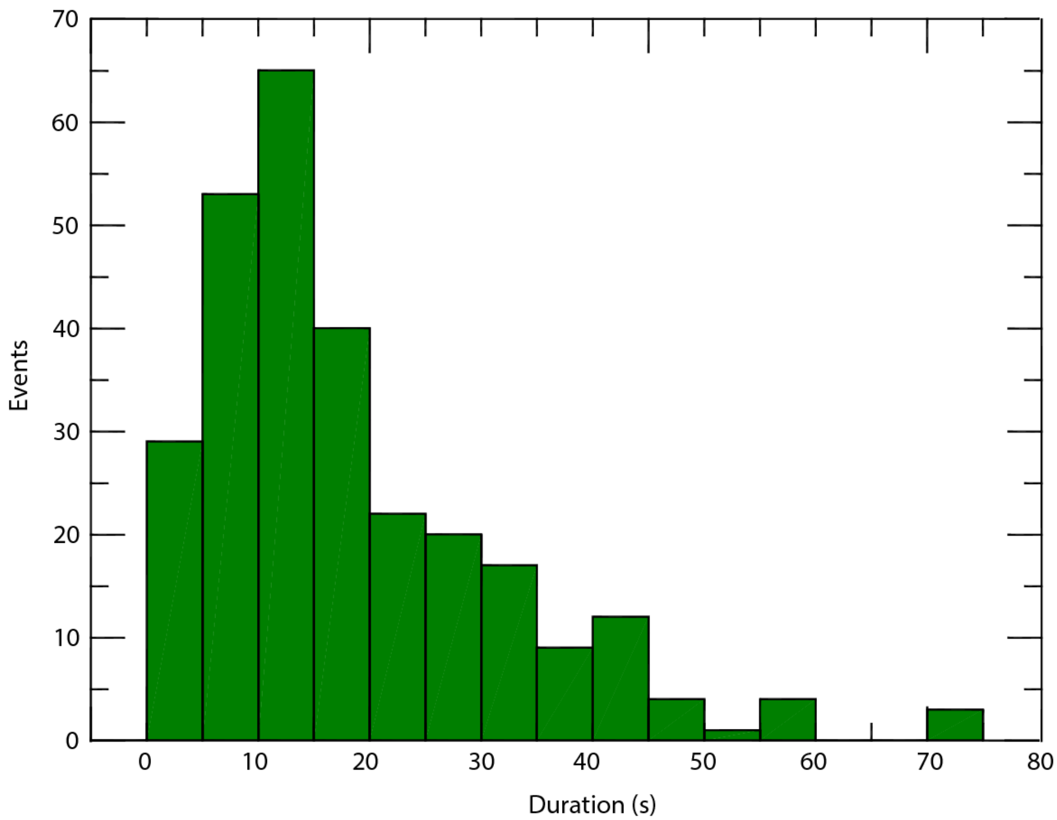

Figure 2. Histogram of the duration of the derivative amplitudes |dB/dt| from both CDR and KJPK for 2015. The bins are 5 s wide and all the events between 70 and 144 s have been combined into one bin.

Table 2. Distribution of "pre- and postmidnight" ≥ 6 nT/s MPEs at two stations (CDR and KJPK) at two different latitudes as a function of time between the most recent substorm onset and event occurrence. "Premidnight" MPEs include those observed between 1700 and 0100 MLT, and "postmidnight" events those between 0200 and 0700 MLT.

Premidnight				
Station	CDR (72.7° CGMLat)		KJPK (64.7° CGMat)	
	# of Events	%	# of Events	%
$\Delta t_{so} \leq 30$ min	105	70	45	57
$30 < \Delta t_{so} < 60$ min	28	19	15	19
$\Delta t_{so} \geq 60$ min	18	12	19	24
Sum	151		79	
Postmidnight				
Station	CDR		KJPK	
	# of Events	%	# of Events	%
$\Delta t_{so} \leq 30$ min	5	71	31	74
$30 < \Delta t_{so} < 60$ min	1	14	5	12
$\Delta t_{so} \geq 60$ min	1	14	6	14
Sum	7		42	

3. The SECS Procedure

The spherical elementary current systems (SECS) technique developed by Amm and Viljanen (1999) uses the horizontal components of vector magnetometer data from an array of ground stations to infer ionospheric equivalent vector currents and current amplitudes (a proxy for field-aligned currents and perpendicular to the ionosphere) in the region covered by the measurements. Weygand et al. (2011) implemented the SECS technique to produce maps of such currents over North America and Greenland, at 10-second cadence from 11 ground arrays: AUTUMNX, CARISMA, CANMOS, DTU, Falcon, GIMA, MACCS, McMAC, STEP, THEMIS, and USGS (Weygand et al., 2009a;b). The spatial resolution of these data are about 1.5° GLat by 3.5° Glong in the current amplitudes and in the equivalent ionospheric currents the spatial resolution is about 3° GLat by 7° Glong. This spatial resolution is driven by the densest distribution of the magnetometers. See Weygand et al. (2011) for more details.

SECS plots of the above quantities were produced for the time of the MPEs identified at two representative stations, Cape Dorset (CDR) and Kuujjuarapik (KJPK). These plots were used to identify the location of MPEs relative to inferred electrojets, the Harang current system, and region 1 and 2 field-aligned currents (**Table 3** presented below). To identify the Harang current system we have examined by eye both the horizontal equivalent ionospheric currents and the vertical current amplitudes. In the equivalent currents we identify a shear between the westward and eastward electrojets where the westward electrojet passes poleward of the eastward electrojet as shown in **Figure 3**. In the current amplitudes we identify for an extended (in longitude) region of upward current with areas of downward current poleward and equatorward of the upward current. A series of SECs maps at a 1-min cadence were also produced around the times of the four case study events presented in section 5.

4. Statistical Analysis

Figure 3 shows a schematic map of the nightside current regions and overlaid ovals showing the dominant locations of "premidnight" and "postmidnight" MPEs. The typical region 1 downward current and region 2 upward current is shown on the dawnside (rightside of the plot) with the westward electrojet in between. The standard region 1 upward current and region 2 downward current is shown on the duskside (left side of the plot) with the eastward electojet in between. At about 23 MLT sits the Harang current system with the upward current system between two areas of downward current and the westward and eastward electrojets.

The left half of **Table 3** lists the number of MPEs observed at CDR and KJPK located beneath the westward electrojet (WEJ), eastward electrojet (EEJ), between the electrojets (Btw), or whether the location is unclear (Unclr). By unclear we mean that the electrojet did not extend longitudinally over several data points and the electrojet values were not well above the values observed equatorward of the auroral oval or the polar cap. Similarly, the right half of the table identifies the overhead current amplitude system in which the MPE occurs: Upward Harang current (UpHar), downward region 1 (DnR1), downward region 2 (DnR2), the boundary between the two (Bdry), upward region 1 (UpR1), upward region 2 (UpR2), and unclear (Unclr). At each station the MPEs are sorted into the same six categories of MLT and time delay after substorm onset as were used in **Table 2**. Also as noted in **Table 2**, the MLT distribution of MPEs was strongly latitude-dependent; only 7 of the 158 MPEs at CDR were in the "postmidnight" category, while 42 of the 121 MPEs at KJPK were in the "postmidnight" category.

Table 3A shows that the vast majority of "premidnight" events at CDR were located beneath the WEJ (133/151 → 88%), with the largest percentages during the first 30 min after substorm onset (91%) then between 30 and 60 min (89%), but decreasing to 68% for MPEs occurring beyond 60 min after substorm onsets. The overhead electrojets could not be clearly identified for the remaining 18 events, but none could be clearly identified as being under the EEJ or clearly between two electrojets.

Approximately half (74/151 → 49%) of the premidnight events at CDR occurred beneath the Harang current system, with little variation between the three time delay categories: 48%, 56%, and 47%, respectively. Of the other vertical current categories, the most common was the downward region 1 current (26%), but again the largest occurrence percentage was during the first 30 min after substorm onset (29%), decreasing to 22%, and 21%, respectively, for the two later categories. Of the remaining categories, 9% occurred under the upward region 2 current and the locations of 12% were unclear.

Table 3B shows that of the few "postmidnight" events observed at CDR, nearly all (6/7 → 86%) were also located under the WEJ, with only one unclear event. None were located under the Harang discontinuity, one under a downward region 1 current, two under an upward region 2 current, and the locations of 4 (57%) were unclear.

Table 3C shows that although the majority of "premidnight" MPEs observed at KJPK (49/79 → 62%) were also located beneath the WEJ, the overall percentage and the percentages in each time delay category (69%, 60%, and 47%) were lower than at CDR. Three events (4%) were located beneath the EEJ, four (5%) between two electrojets, and the location of 23 (29%) was unclear. A location beneath the Harang current system was the most common for "premidnight" MPEs observed at KJPK (33%), but other locations were also often identified: 25% under an upward region 2 current, 16% under a downward region 1 current, and 8% under a downward region 2 current. The locations of 13/79 → 16% were again unclear.

Table 3D shows that "postmidnight" MPEs at KJPK were associated with the WEJ even more strongly (37/42 → 88%) than the "premidnight" ones (62%). The locations beneath the ionospheric currents of the five remaining MPEs, all in the 0-30 min time delay category, were unclear. As was the case for CDR, none of the "postmidnight" MPEs at KJPK were located beneath the upward Harang current system. The most common location was beneath the upward region 2 current (60%), followed by the downward region 1 current (24%), and at the boundary between two vertical currents (7%). The locations of 10% were again unclear.

Table 3. SECS location identifications for "Premidnight" (before 1 MLT) and "Postmidnight" (after 2 MLT) MPEs >6 nT/s observed at Cape Dorset (CDR) and Kuujjuarapik (KJPK) during 2015 and 2017.

Δt	Tot	WEJ	EEJ	Btw	Unclr	UpHar	Dn R1	Dn R2	Bdry	Up R1	Up R2	Unclr
A. Cape Dorset Premidnight												
0-30	105	96	0	0	9	50	30	0	3	0	10	12
30-60	27	24	0	0	3	15	6	0	2	0	1	3
>60	19	13	0	0	6	9	4	0	1	0	2	3
Total	151	133	0	0	18	74	40	0	6	0	13	18
B. Cape Dorset Postmidnight												
0-30	5	5	0	0	0	0	1	0	0	0	1	3
30-60	1	0	0	0	1	0	0	0	0	0	0	1
>60	1	1	0	0	0	0	0	0	0	0	1	0
Total	7	6	0	0	1	0	1	0	0	0	2	4
C. Kuujjuarapik Premidnight												
0-30	45	31	2	4	8	19	11	3	0	1	7	4
30-60	15	9	1	0	5	1	1	3	0	0	6	4
>60	19	9	0	0	10	6	1	0	0	0	7	5
Total	79	49	3	4	23	26	13	6	0	1	20	13
D. Kuujjuarapik Postmidnight												
0-30	31	26	0	0	5	0	6	0	3	0	18	4
30-60	5	5	0	0	0	0	3	0	0	0	2	0
>60	6	6	0	0	0	0	1	0	0	0	5	0

Total	42	37	0	0	5	0	10	0	3	0	25	4

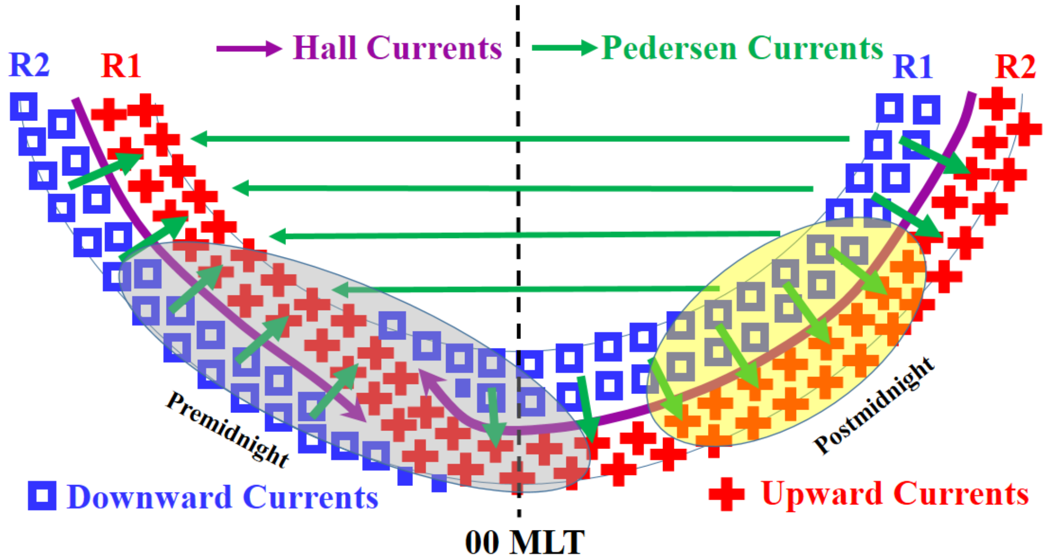

Figure 3. Schematic diagram of the midnight region field aligned, Hall, and Pedersen currents. The blue squares indicate current into the ionosphere, and the red '+' symbols indicate the current out of the ionosphere. The mauve arrows show the eastward and westward electrojets and the green arrows display the Pedersen currents. The black dashed line demarks magnetic midnight. The gray and yellow ovals indicate the premidnight and postmidnight regions where the MPEs generally occurred.

5. Example Events:

In this section we present four intervals of MPE activity: 7 April 2015, 19 April 2015, 23 March 2017, and 16-17 June 2017. The 7 April 2015 event is a typical MPE at high latitude during a substorm. The 19 April 2015 MPE is a typical MPE at lower latitude during a non-substorm with ASIs. The 23 March 2017 event occurs within an unclear current system but ASIs are available. The 16-17 June 2017 period is an unusual period with repeating MPEs covering both a substorm and non-substorm period. In each case we show an 8-hour interval of ground magnetometer data from CDR, INUK, or KJPK, along with simultaneous traces of the SML and SMU indices and the Bz component of the IMF. We also present SECS maps of the current amplitudes and the equivalent ionospheric currents over northern North America and western Greenland about one minute before and at the time of the MPE, respectively. In two of the four intervals THEMIS auroral imager data over KJPK were available and images near the time of the MPE are shown for each event. Movies of the imager data covering a longer time interval are provided in the Supplemental Information.

5.1. 7 April 2015 MPE Observed at Cape Dorset at 02:23 UT

This MPE event occurred at 21:26 MLT after an extended period of quiet geomagnetic conditions and this event is a typical MPE at high latitude during a substorm. The SYM/H index varied between -15 and 0 nT from 00:00 UT April 6 to 10:00 UT April 7, and during this same time interval the solar wind speed fell nearly monotonically from 500 km/s to 420 km/s and the solar wind dynamic pressure was consistently below 2 nPa (based on OMNI data time-shifted to the nose of the Earth's bow shock). This MPE occurred at CDR 7 minutes after an isolated substorm onset at 02:17 UT (Ohtani and Gjerloev, 2020) under a westward electrojet and a localized region of upward current following a 40-minute interval when |SML| was on the order of 50 nT.

Panels a-c of **Figure 4** show the time series of the magnetic field observed at CDR during an 8-hour interval centered approximately at the time of this MPE. Panels d-f show the SML and SMU indices and the Bz GSM component of the propagated OMNI IMF data, respectively. The IMF Bz data has been time-shifted from the upstream L1 libration point to the nose of the Earth's bow shock. All three components of the magnetic field at CDR were nearly constant before 02:15 UT, at which time Bx and By began to drop by nearly 300 nT and Bz began to rise ~250 nT. At 02:23 UT the Bx component reached its minimum value, By experienced a short >100 nT spike, and Bz returned to its previous level before going negative by ~300 nT. The largest derivative, +6.8 nT/s, appeared in the Bx component at about 02:24 UT as it returned to approximately its value before the MPE.

The SML index began to drop near 02:17 UT and dropped ~200 nT by 02:22 UT before briefly retreating and stabilizing near -20 nT until 02:40 UT, but the SMU index showed only ± 50 nT variability during the same interval. The IMF Bz component was negative from 01:17 to 02:05 UT, then rose to slightly above 0 nT between 02:05 and 02:17 UT before decreasing to -1 nT during the last 7 minutes before the MPE occurred.

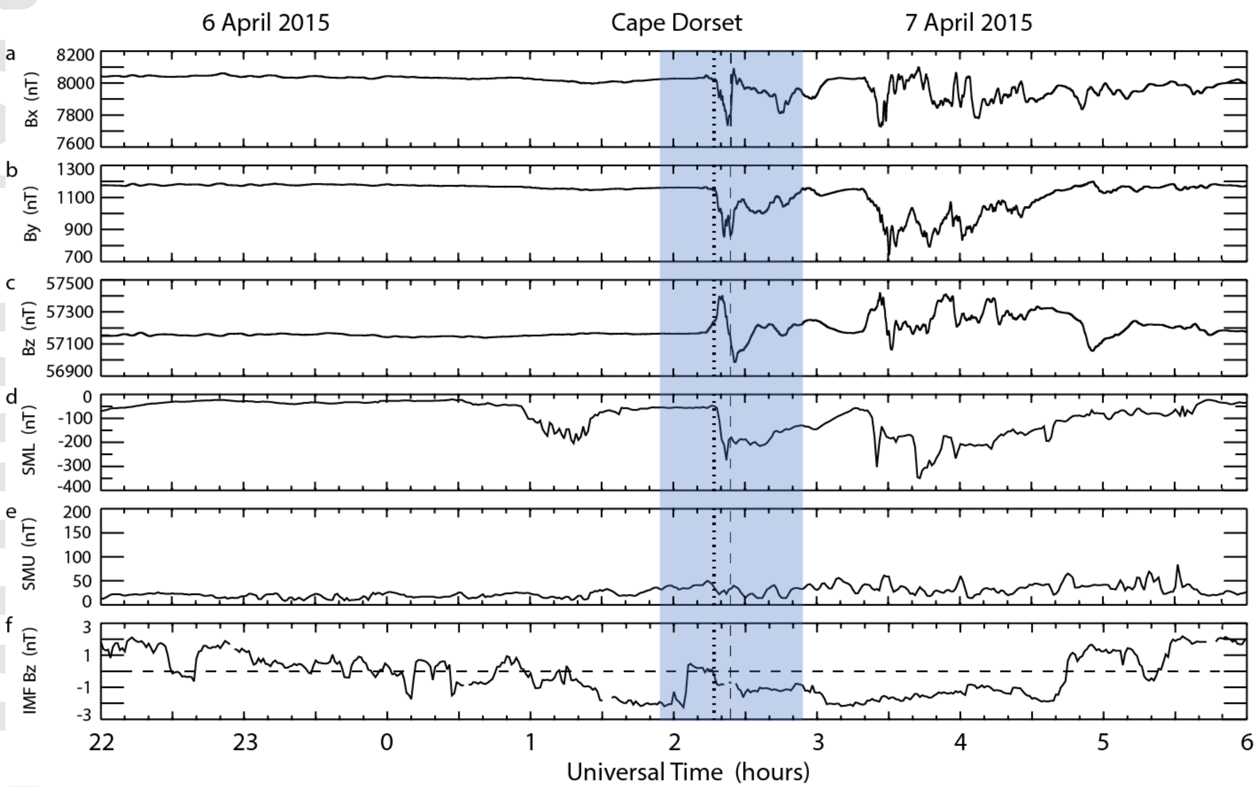

Figure 4. Plot of three components of the magnetic field observed at Cape Dorset (panels a-c), the SML and SMU indices (panels d-e), and the Bz GSM component of the IMF (panel f) from 22 to 24 h UT on 6 April 2015 and from 0 to 6 h UT on 7 April 2015. The time of the MPE,

02:24 UT, is indicated by the vertical dashed line, and the time of the identified substorm onset at 02:17 UT is indicated by the vertical dotted line.

The four panels of **Figure 5** show SECS maps of Northern North America and Western Greenland at 02:15, 02:19, 02:24, and 02:25 UT. Geomagnetic activity was quiet (SML of about~-50 nT) over most of North America from 02:00 UT through 02:10 UT, with only modest activity visible until 02:15 UT, when a weak northwesterly electrojet appeared at CDR. At 02:17 UT a weak northwesterly electrojet appeared at INUK, and weak localized upward and downward current regions began to appear north and south, respectively of INUK, but there was no activity to the north of CDR. The downward current regions expanded to the west at 02:18 UT then intensified slightly, while a second small region of weak upward current appeared at the west end of Hudson Bay. The northwesterly electrojet at CDR gradually increased through 02:19 UT and rotated to the west. At 02:19 UT the upward current over SALU intensified and the downward current region to the north of CDR also intensified and became more extended in longitude. CDR was at this time located under the region between the two vertical currents. Both the downward and upward current regions gradually moved poleward, and CDR remained between these regions from 02:19 through 02:23 UT, but the horizontal current intensified significantly (from to 374 mA/m at 02:19 to 601 mA/m at 02:23 UT) and at the same time the downward and upward currents bracketing the horizontal current enhanced over a limited area. The Bz component in **Figure 4** shows a bimodal variation with its sign changing around the negative peaks of Bx and By. This strongly suggests that a strong current passed over the station, and the associated magnetic variation was more spatial than temporal. However, the maps of ionospheric currents do not show this motion but this bimodal variation may occur at spatial scales smaller than the SECs can resolve. Beginning at 02:24 UT the upward current region moved over CDR and by 02:25 UT the horizontal current at CDR had dropped from 493 mA/m to 334 mA/m and had rotated to the northwest. See the yellow circled region in **Figure 5**.

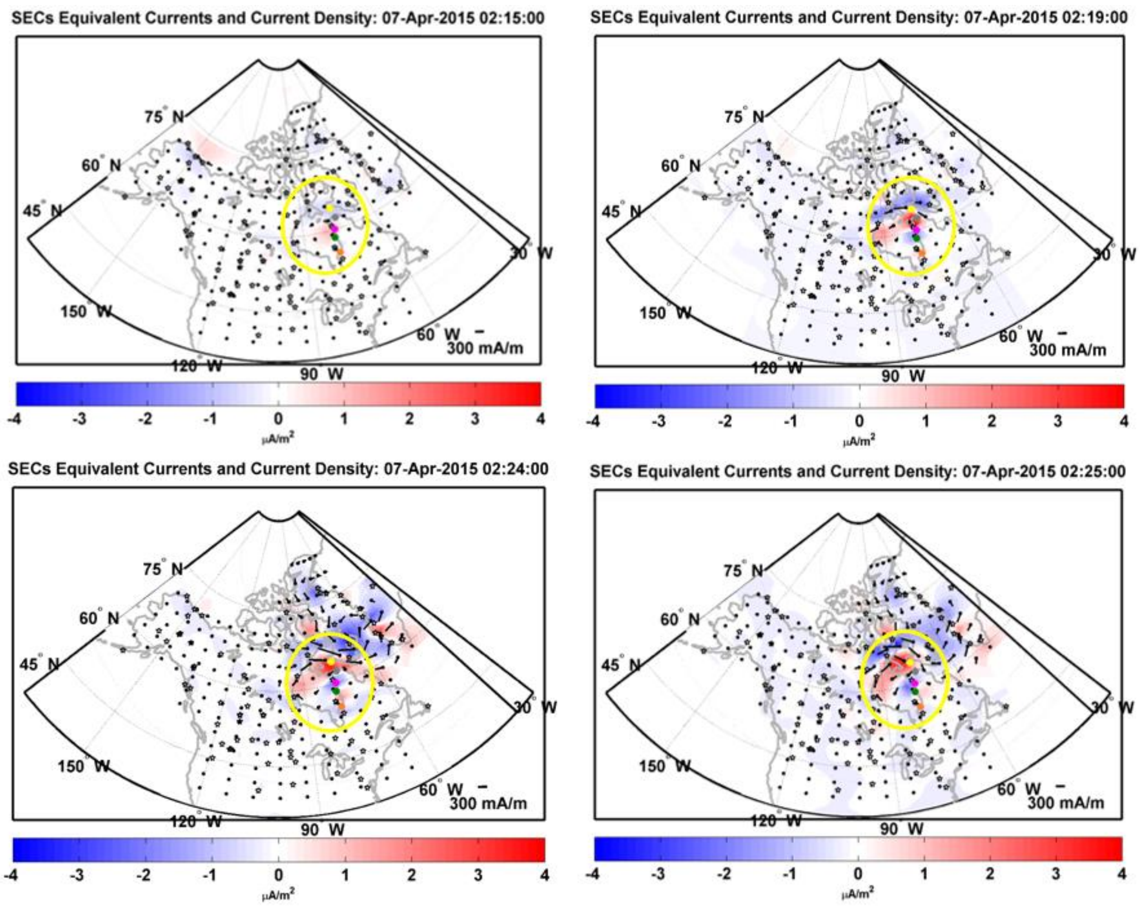

Figure 5. SECS maps of horizontal equivalent currents (black vectors without arrow heads originating at grid points indicated by black dots) and vertical current amplitudes (with intensity and sign given in the color bar at the bottom). The vertical black solid line marks geographic midnight. Panels a through d are SECS maps for 02:15, 02:19, 02:24 and 02: 25 UT 7 April 2015, respectively.

5.2. 19 April 2015 MPE Observed at Kuujjuarapik at 4:10 UT

This MPE event occurred at 23:04 MLT during the late recovery phase of a geomagnetic storm that reached a minimum SYM/H of -88 nT at 23:40 UT April 16, 2015. At the time of the MPE the SYM/H index was -26 nT, the solar wind flow speed was 453 km/s, and the solar wind dynamic pressure was 1.8 nPa. Panels a-c of **Figure 6** show the time series of the magnetic field components observed at KJPK during an 8-hour interval centered approximately at the time of this MPE. At 04:10 UT short negative spikes appeared in all three components of the KJPK magnetic field; the largest derivative, -9.7 nT/s, appeared in the Bz component.

Panels d-f of **Figure 6** show the SML and SMU indices and the Bz component of the IMF, respectively. This MPE event also occurred close in time to a rapid drop in the SML index that followed several hours of moderate activity of about 200 nT from about 02:10 UT to ~04:00 UT. The SML index began to drop near 4:08 UT and decreased ~200 nT by 04:12 UT before briefly increasing, and the SMU index rose by ~50 nT. The IMF Bz component remained negative for over 4 hours but rose toward 0 nT during the last 8 minutes before the MPE occurred.

All three of the substorm lists (Newell and Gjerloev, 2011; Forsyth et al., 2015; and Ohtani and Gjerloev, 2020) available for this date on the SuperMAG products web site (https://supermag.jhuapl.edu/substorms/) noted a substorm onset at about 00:30 UT, nearly 4 hours prior to the MPE. However, the list compiled by Forsyth et al. (2015) included a substorm onset at 04:09 UT. The decrease in SML at 04:09 UT was short-lived, and did not satisfy the sustained-drop criteria listed in the other two papers. If the drop in SML at 04:09 UT was not a substorm onset in Newell and Gjerloev (2011) and Ohtani and Gjerloev (2020), then the event was either an intensification, which is difficult to identify using only SML, or a pseudobreakup and most likely due to the short duration of the event.

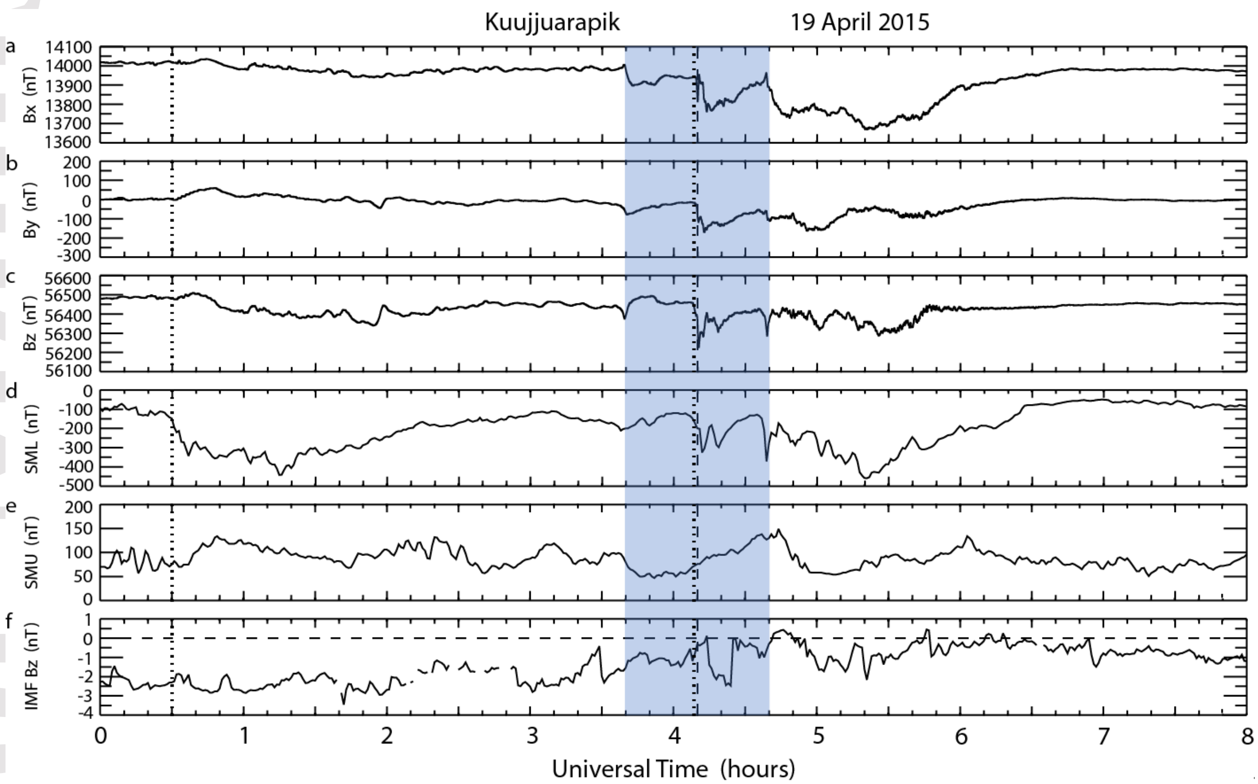

Figure 6. Plot of three components of the magnetic field observed at Kuujjuarapik (panels a-c), the SML and SMU indices (panels d-e), and the Bz GSM component of the IMF (panel f) from 0 to 8 h UT on 19 April 2015. The time of the MPE, 4:10 UT, is indicated by the vertical dashed line, and the times of identified substorm onsets at 00:30 UT and 04:09 UT are indicated by vertical dotted lines.

Figures 7a and 7b show SECS maps of Northern North America and Western Greenland at 04:09 and 04:10:30 UT, respectively. The pattern of both equivalent ionospheric currents and current amplitudes in the region near KJPK remained virtually constant from 04:00 (not shown) to 04:09. Two relatively localized and moderate regions of current amplitudes were visible at the western edge of the black circle, which represent the field of view of the KUUJ all sky camera, at 04:09 UT: a localized upward current between INUK and SALU (north of KJPK) along with a similarly localized downward current between INUK and KJPK, and a localized WEJ extending west of SALU. No horizontal current was visible near KJPK at this time. We note that the structure appears to have a FAC-like current of one direction in the middle and two FACs of opposite direction in adjacent regions. This structure is similar to FACs in Alfven resonance. By 04:10:30 UT both the upward and downward vertical currents had moved rapidly southward and intensified, and a westward electrojet that was narrow in latitude but extended in longitude both east and west appeared above INUK and KJPK.

The lower panels of **Figure 7** show four auroral images obtained by the THEMIS auroral imager at Kuujjuaq that show the rapid appearance and slightly slower westward motion of an east to west auroral arc that extended over Inukjuaq by 04:10:15 UT (labelled red dot NNW of Kuujjuarapik) (Labels for these stations as well as Salluit, Puvurnituq, Sanikiluaq, and Cape Dorset are shown in **Figure 7c1**.) The rapid development of undulations in what was at first a nearly linear auroral arc suggests some instability may be occurring in the magnetotail. The location of this arc, at least at 4:10 UT, was between the Harang upward current and the downward region 1 currents. It would thus map approximately to the inner edge of the plasma sheet, where an instability is likely. We note also that the ΔBx and ΔBy perturbations associated with this MPE at KJPK, INUK, and PUVR were all negative, but the ΔBz perturbations differed; ΔBz was negative at KJPK, bipolar and equal up and down at INUK, and positive at PUVR. The variation of the ΔBz fluctuations is the result of a westward electrojet forming between INUK and KJPK at about 04:09:40 UT and then strengthening and widening poleward over INUK by 04:10:10 UT.

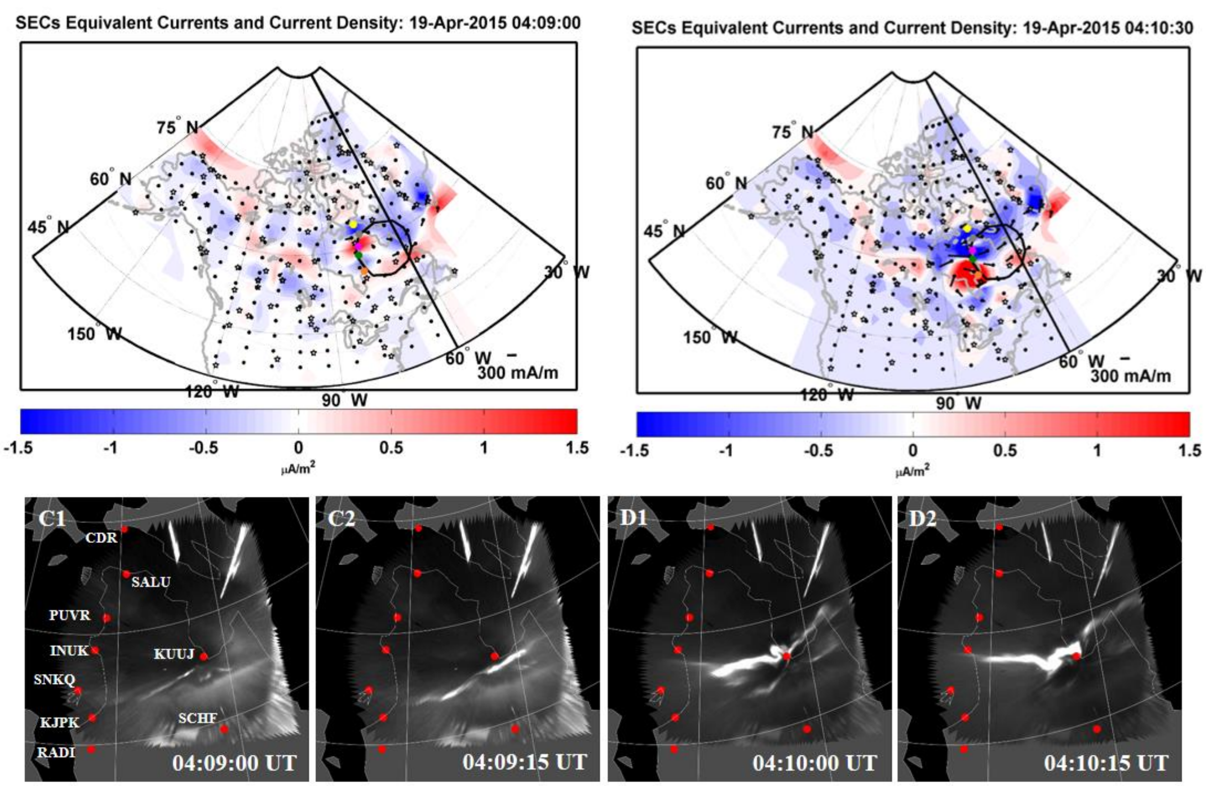

Figure 7. Panels a and b are SECS maps for 04:09 and 04:10:30 UT 19 April 2015. The black circle indicates the field of view of the KUUJ all sky camera. Panels c1 – d2 are auroral images

obtained by the THEMIS imagers at Kuujjuaq: c1 and c2 at 04:09:00 and 04:09:15 UT, and d1 and d2 at 04:10:00 and 04:10:15 UT, respectively.

5.3. 23 March 2017 MPE Observed at Inukjuak at 01:18 and 01:35 UT

A 6.4 nT/s MPE observed at KJPK at 01:18 UT located at 20:02 MLT was included in our statistical survey, but analysis of data during this interval from nearby stations quickly revealed that two MPEs with much larger amplitude were recorded at INUK, just north of KJPK. These two MPE events occurred during the early recovery phase of a weak geomagnetic storm that reached a minimum SYM/H of -46 nT at 23:37 UT March 22, 2017. The SYM/H index was -36 nT at 01:18 UT during the first MPE and -29 nT at 01:35 UT on March 23 for the second MPE. The solar wind flow speeds at these times were 635 km/s and 641 km/s, and the solar wind dynamic pressures were 1.2 nPa and 1.1 nPa, respectively. The three substorm lists again disagreed regarding substorm onsets prior to this MPE. No substorm onset during the 8-hour interval shown was included in the Ohtani and Gjerloev (2020) substorm list, but this list consists of only isolated substorms. The last substorm onset on March 22 identified in the Newell and Gjerloev (2011) and Forsyth et al. (2015) lists was at 23:23 UT, about 2 hours prior to the first MPE. Both the Newell and Gjerloev (2011) and Forsyth et al. (2015) lists included onsets near 01:22 UT March 23 shortly after the first MPE, but no onset was identified near the time of the second MPE. An onset was also identified at 00:17 UT on March 23 in the Forsyth et al. (2015) list.

Panels a-c of **Figure 8** show the time series of the magnetic field observed at INUK during the 8-hour interval between 21:00 UT March 22 and 05:00 UT March 23. In contrast to the general correlation between MPE and SME perturbations in the two previous intervals, **Figure 8d** shows that the SML index was nearly constant at about -200 nT during the 25 minutes prior to, during, and for another 15 min after the first MPE. It then dropped sharply to -500 nT at the time of the second MPE. The SMU index (**Figure 8e**) was at or below 100 nT during the 30 min prior to the first MPE, rose gradually to 150 nT over the next 10 min, and fell back to 100 nT at the time of the second MPE. The IMF Bz component was again negative for most of the 4 hours prior to the MPE, but dropped from +1 to -2 nT during the 13 minutes before the time of the first MPE and dropped again to near -2 nT about 2 min before the second MPE.

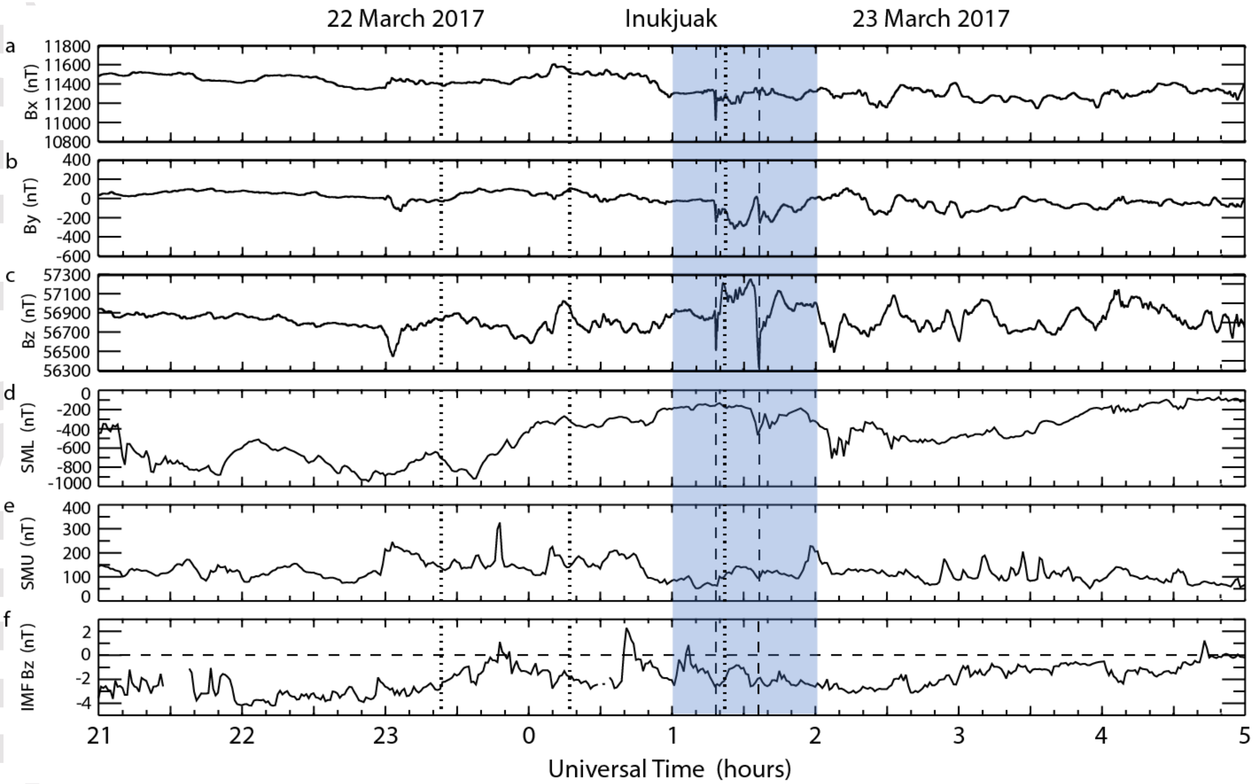

Figure 8. Plot of three components of the magnetic field observed at Inukjuak (panels a-c), the SML and SMU indices (panels d-e), and the Bz GSM component of the IMF (panel f) from 21 UT on 22 March 2017 to 5 h UT on 23 March 2017. The times of the MPEs, 01:18 and 01:36 UT on 23 March 2017, are indicated by the vertical dashed lines, and the times of identified substorm onsets at 23:23 UT, 00:17 UT, and 01:22 UT are indicated by vertical dotted lines.

Both of the MPEs at INUK during this interval had the largest derivatives in the Bz component (-29.5 nT/s at 01:18 UT and +13.3 nT/s at 1:36 UT), but they exhibited different signatures in the Bx and By components. In order to put these differences in context, **Figure 9** and **Table 4** show information from six of the seven stations (CDR, SALU, PUVR, INUK, KJPK, and RADI) that were aligned approximately along a north-south line. See **Figure 1**. Unfortunately, no data were available from SNKQ on this day.

Figure 9 shows the traces of each component at these stations between 01:00 and 01:40 UT. During the first MPE, a sharp ~300 nT negative spike in the Bx component appeared at INUK and a weaker ~100 nT negative double-minimum spike in Bx appeared at PUVR. At the same time a ~100 nT positive spike in Bx appeared to the south at KJPK and a weaker ~50 nT spike in Bx appeared at RADI; at both stations they were followed by a more gradual decrease to lower values over the next 6 min. Only very small perturbations appeared to the north at CDR and SALU. At the same time smaller negative perturbations appeared in the By components at PUVR, INUK, and KJPK; the By values at PUVR and INUK returned toward their original levels after ~3 min, but at KJPK and RADI they continued downward 3-4 minutes before rebounding slightly. A steep ~450 nT negative spike in Bz appeared at INUK, a weaker, more gradual ~200 negative spike in Bz arose at KJPK, and a very weak and gradual drop appeared at

RADI. The three stations north of INUK observed positive excursions in Bz: a ~200 nT step at PUVR, a ~100 nT step at SALU, and a very weak, gradual rise at CDR.

Perturbations caused by the second MPE extended more widely and were shifted slightly to the north, with negative Bx pulses at CDR, SALU, and PUVR, two small bipolar Bx pulses at INUK, and positive Bx pulses at KJPK and RADI. The largest perturbation in By was a bipolar pulse at PUVR; negative spikes appeared to the north at CDR and SALU, and positive pulses appeared with successively decreasing amplitude at INUK, KJPK, and RADI. Perturbations were largest in the Bz component at nearly all stations: initially positive excursions at CDR and SALU, large negative spikes at PUVR and INUK, and more gradual positive excursions with successively decreasing amplitude at KJPK and RADI.

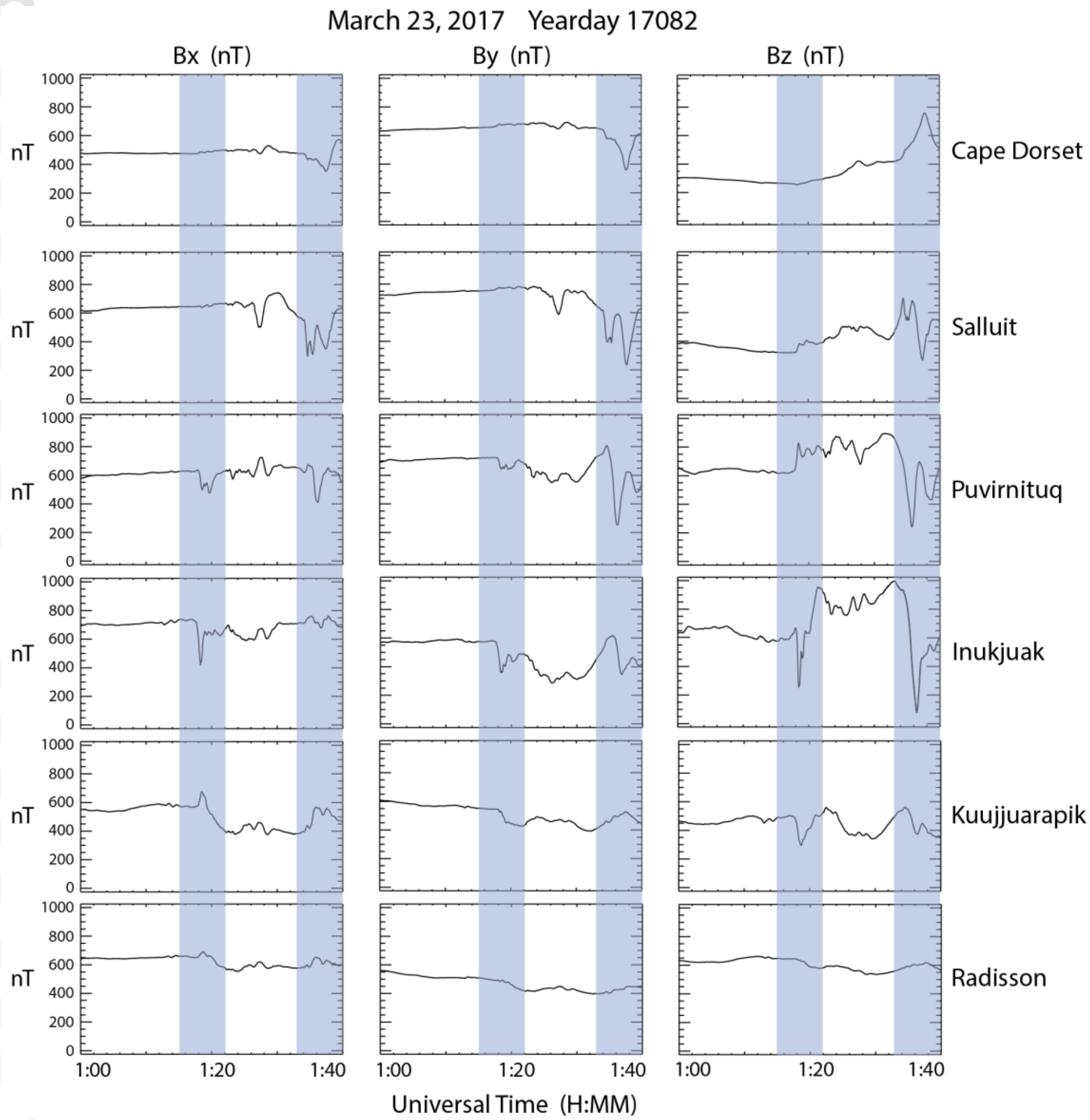

Figure 9. Plots of the Bx, By, and Bz components of the magnetic field measured at Cape Dorset, Salluit, Puvurnituq, Inukjuak, Kuujjuarapik, and Radisson, arranged in MLAT from highest to lowest, between 1:00 and 1:40 UT 23 March 2017. The shaded areas outline the time intervals of MPEs near 1:18 and 1:35 UT.

Table 4 lists the maximum derivatives in each component observed at these stations and also lists the great circle distance between successive pairs of stations. The derivatives during the first event were more localized in latitude, with very small values in all 3 components at CDR, SALU, and RADI, with the largest amplitudes in all components at INUK, and with an approximately symmetric falloff to both the north (PUVR) and south (KJPK). In contrast, the horizontal derivative components during the second event exceeded 10 nT/s at both SALU and PUVR (to the north), although the vertical components exceeded 10 nT/s at SALU, PUVR, and INUK and had approximately equal amplitude.

We note that the relative magnitudes of the largest perturbations in the magnetic field shown in **Figure 9** did not compare closely to the largest derivatives listed in **Table 4**. For example, the ratio of maximum dBz/dt values at INUK for the two events was (29.5 nT/s / 13.3 nT/s) = 2.22, while the corresponding ratio of ΔBz perturbations was (406 nT / 854 nT) = 0.48. This lack of good proportionality between ΔB perturbations and dB/dt values during the large MPEs was earlier pointed out by Viljanen (1997), Viljanen et al. (2006); and Engebretson et al. (2019a). It can be attributed to two MPE characteristics: their short duration relative to the full ΔB excursion, and their greater variability in direction.

Table 4. Maximum derivatives in each component of the magnetic field measured at CDR, SALU, PUVR, INUK, KJPK, and RADI during the MPEs observed near 1:18 and 1:35 UT on 23 March 2017. In cases when both positive and negative derivatives exceeded 10 nT/s, both are shown. Also shown are the great circle distances between next-neighbor pairs of these stations.

Station	Time (HH:MM)	dBx/dt	dBy/dt	dBz/dt
CDR	01:18 UT	0.7	0.6	0.4
SALU	01:18 UT	-0.8	-0.5	2.4
PUVR	01:18 UT	-7.8	-4.5	8.5
INUK	01:18 UT	13.6/-13.0	-8.1	21.3/-29.5
KJPK	01:18 UT	-4.9	-2.7	-6.4
RADI	01:18 UT	1.2	-1	-1.0
CDR	01:35 UT	3.7	4.8	3.1
SALU	01:35 UT	-12.3	-10.0	-11.8
PUVR	01:35 UT	-10.9	-13.2	13.1
INUK	01:35 UT	3.4	-7.2	13.3/-12.5
KJPK	01:35 UT	5.5	1.3	-3.5
RADI	01:35 UT	2.3	0.9	0.7

Station Pair	Distance
CDR-SALU	228 km
SALU-PUVR	261 km
PUVR-INUK	173 km
INUK-KJPK	356 km
KJPK-RADI	167 km

Panels a and b of **Figure 10** show the SECS maps for two minutes just before and at the time of the 01:18 UT MPE on this day. The horizontal and vertical currents near PUVR, INUK, and KJPK were near 0 mA/m and changed little from 01:05 UT (not shown) to 1:17 UT. At 01:18 UT a horizontal current going WNW suddenly appeared at INUK under the northern edge of a still rather weak downward current, and a weak upward current appeared between INUK and KJPK. Beginning at 01:19 UT and extending until 01:25 UT the region of upward current moved slightly northeast from INUK and gradually strengthened (not shown).

Despite the relatively low SML and SMU values, considerable auroral activity was observed before, during, and after the occurrence of this MPE. A relatively quiet E-W arc appeared between SNKQ and INUK between 01:03 and 01:10. This arc broke up at 01:13 UT and re-formed just south of INUK at 01:15 UT (**Figure 10c** shows this arc at 01:16:30 UT). The second arc faded at 1:17 UT but brightened explosively (a major intensification) at 01:17:45 UT above INUK (**Figure 10d**). There was some considerably weaker auroral activity poleward of these stations in the SNKQ all sky imager field of view for the next 10 min, and at 01:26 and 01:29 UT two streamers moved rapidly from the north to south in between SNKQ and INUK, but no MPEs associated with these streamers reached 6 nT/s.

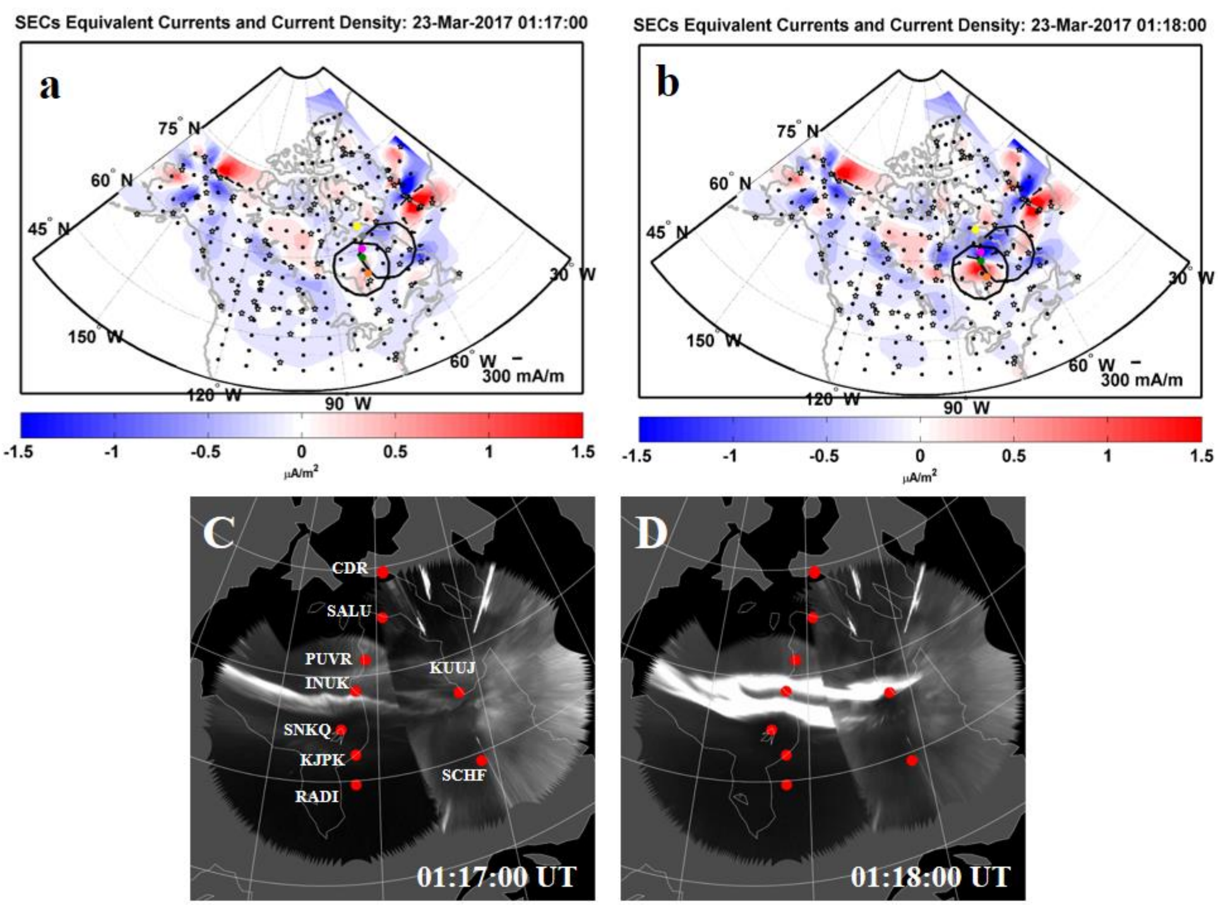

Figure 10. Panels a and b are SECS maps for 01:16:30 and 01:18 UT March 23, 2017, respectively, as in **Figure 7**. The black circles in the SECS maps indicate the field of view of the

SNKQ and KUUJ all sky cameras. Panels c and d are composites of auroral images obtained by the THEMIS imagers at Sanikiluaq and Kuujuaq at 01:17 and 01:18 UT.

The second MPE event near 01:35 UT located at 20:19 MLT was associated with more intense currents and auroral activity over northeastern Arctic Canada from 01:29 to past 01:40 UT. However, the progression of SECS maps before and during this event showed that only downward currents appeared over an extended region above western Quebec between 01:29 and 01:34 UT, and between 01:33 and 01:34 UT these currents were weak or nonexistent in the localized region from SALU to INUK. Panels a and b of **Figure 11** show SECS maps for two minutes just before and at the time of the MPE on this day. At 01:35 UT an intense region of upward current appeared suddenly in this localized region (**Figure 11b**) and gradually diminished in intensity to 01:39 UT.

Auroral images before and during this event showed that after an interval of only faint auroras overhead of these stations from 01:31 to 01:34 UT (e.g., **Figure 11c**: 01:33), beginning at 01:34:45 UT an intense and wide streamer moved into the field of view from the northeast. By 01:36:30 UT it extended over SALU, PUVR, INUK, and as far as SNKQ (**Figure 11d**: 01:36:30 UT); it then became stationary and began to fade away.

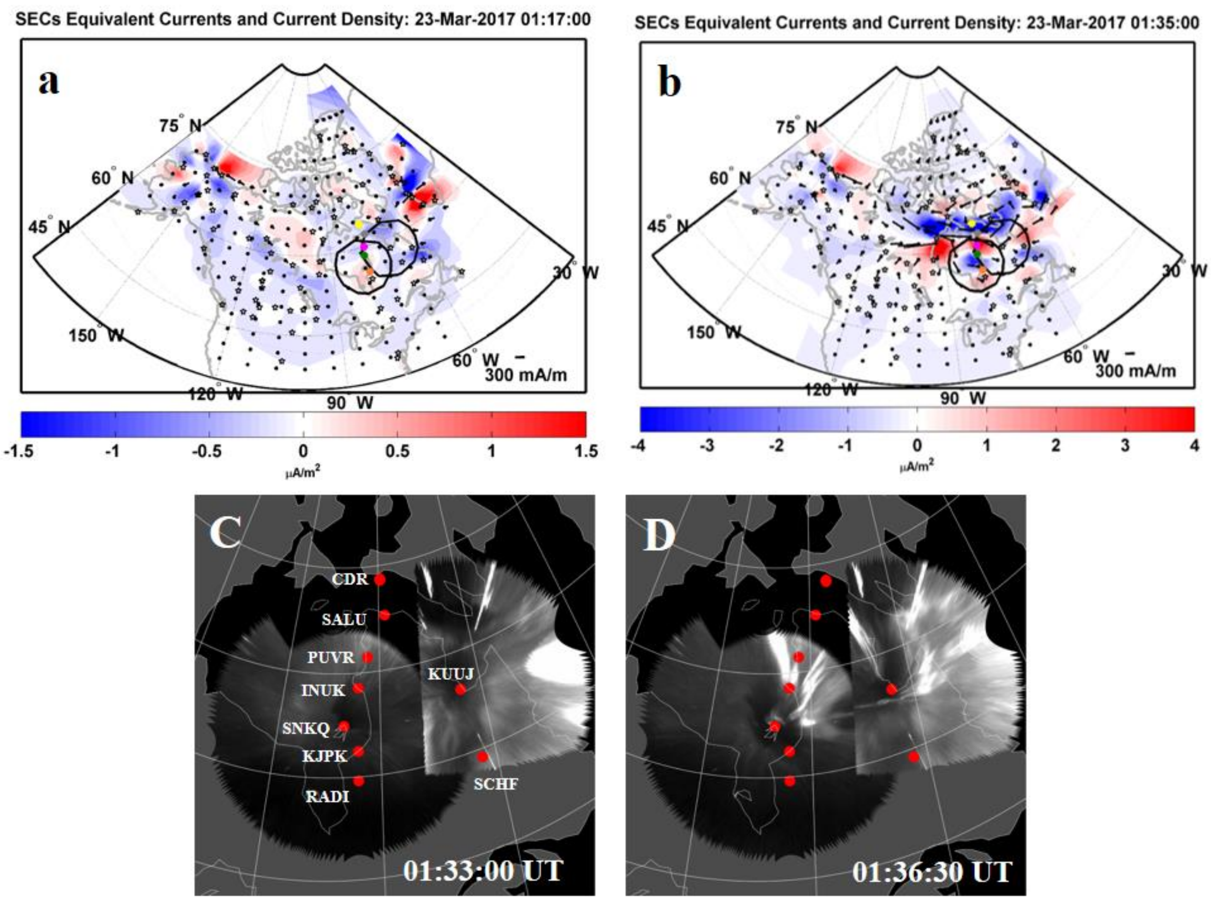

Figure 11. Panels a and b are SECS maps for 01:33 and 01:35 UT 23 March 2017, respectively, as in Figure 6. The black circles indicate the field of view of the SNKQ and KUUJ all sky

cameras. Panels c and d are mosaics of auroral images obtained by the THEMIS imagers at Sanikiluaq and Kuujjuaq at 01:33 and 01:36:30 UT.

5.4. June 16-17, 2017 Five MPEs Observed at Kuujjuarapik

Figure 12 shows solar wind and interplanetary magnetic field parameters between 00:00 UT 16 Jun 2017 and 04:00 UT 17 Jun 2017, propagated to the nose of the Earth's bow shock, as obtained from the OMNI database at https://cdaweb.gsfc.nasa.gov/cgi-bin/eval1.cgi. This period resembles a co-rotating interaction region based on the solar wind speed and density. Increases in the interplanetary magnetic field magnitude (**Figure 12a**), solar wind velocity (Vsw, **Figure 12e**), solar wind density (Nsw, **Figure 12f**), and the solar wind dynamic pressure (Psw, **Figure 12g**) began gradually near 03:00 UT on June 16. The solar wind speed increased from ~300 km/s to ~400 km/s by 04:00 UT, and exhibited two jumps, near 08:40 and 18:00 UT on June 16, peaking at 650 km/s near 19:00 UT before gradually falling to 470 km/s by 04:00 UT June 17. Dynamic pressure reached ~20 nPa near 07:55 UT, dropped rapidly to ~4 nPa by 08:40 UT, and was steady near 3 nPa from ~18:00 UT June 16 to 04:00 June 17 (**Figure 11g**). The interplanetary magnetic field magnitude (**Figure 12a**) continued to rise to ~15 nT at 11:00 UT before gradually dropping to ~7 nT by 18:00 UT, after which it remained fairly steady in magnitude even while all three IMF components continued to exhibit large fluctuations (**Figures 12b**, **c**, and **d**). The SYM/H index (**Figure 12h**) roughly followed the dynamic pressure in its gradual rise and rapid fall between 03:00 and 08:40 UT. During the subsequent main phase of a weak magnetic storm it dropped unsteadily to -38 nT near 00:00 UT June 17 and subsequently began an equally unsteady modest recovery phase through all of June 17 (not shown). The MPEs to be discussed in this section occurred in the shaded region at the right of **Figure 12**, between 20:00 UT June 16 and 04:00 UT June 17, as shown in **Figure 13**. At the time of the first MPE at 22:37 UT on June 16, SYM/H was -26 nT, and at 01:14, 01:28, 01:42, and 01:54:30 UT on June 17 SYM/H was -29, -26, -25, and -27 nT, respectively.

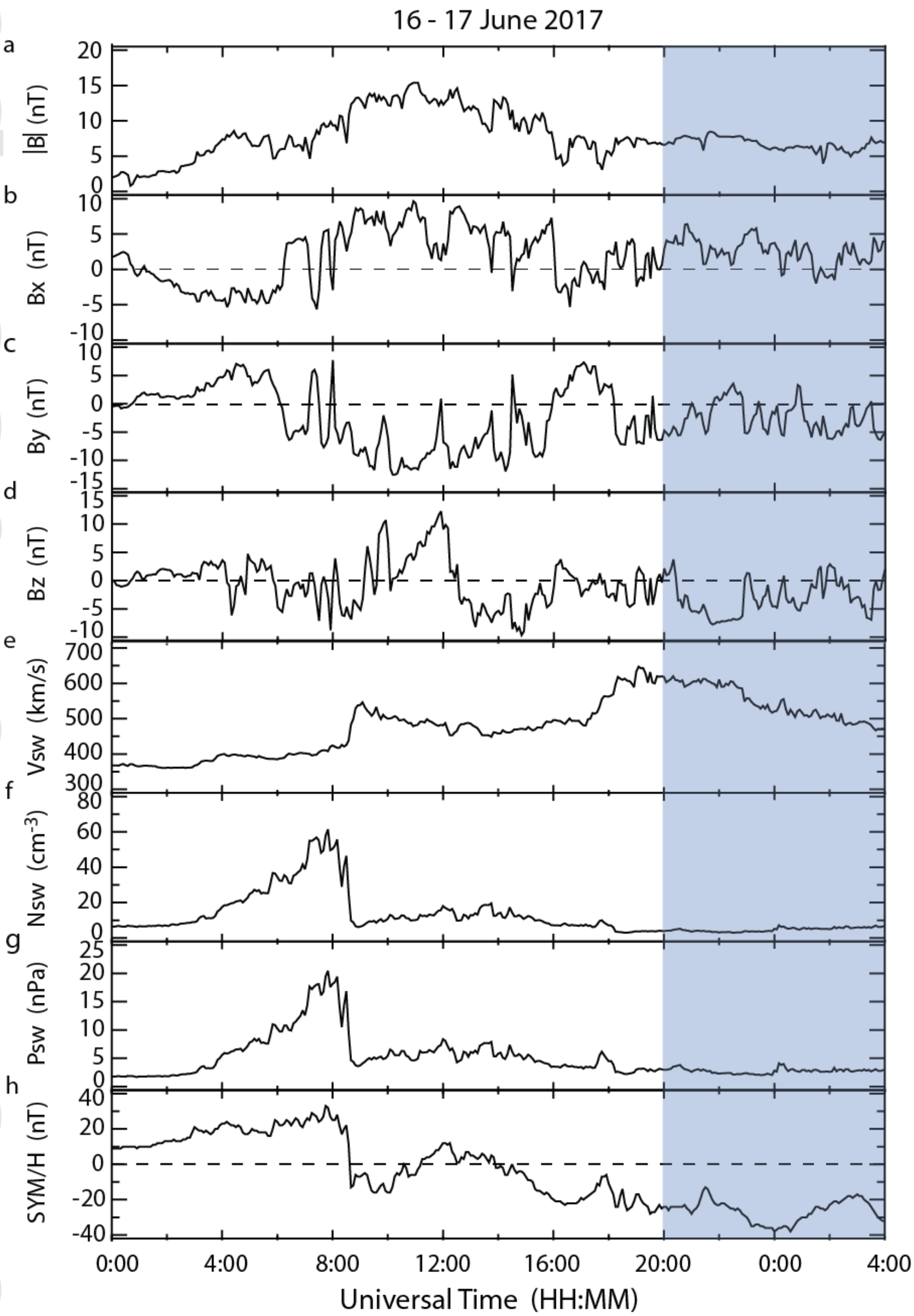

Figure 12. OMNI IMF and solar wind data (panels a-g), and the SYM/H geomagnetic activity index (panel h) from 00:00 16 Jun 2017 to 04:00 UT 17 Jun 2017. Panel a shows the IMF magnitude |B|, panels b-d show the sunward, east-west, and north-south GSM components of the IMF (Bx, By, and Bz), panel e shows the solar wind flow speed (Vsw), panel f shows the solar wind proton number density (Nsw), and panel g shows the solar wind dynamic pressure, all propagated to the nose of the Earth's bow shock. The shaded region at the right includes the times of the five MPEs discussed in this section.

Figure 13, in the same format as **Figures 4**, 6, and 8, shows observations from KJPK and the OMNI database from 20:00 UT 16 Jun 2017 to 04:00 UT 17 Jun 2017. More intense MPEs were observed at neighboring stations, as discussed below in **Table 5**, but the magnetic field variations at KJPK were representative of the set. The MPE at KJPK shown in **Figure 13** at 22:37 UT on 16 June occurred 18 minutes after a substorm onset (identified only in the Newell and Gjerloev (2011) substorm list at 22:19 UT), 8 minutes after the SML index reached a minimum value near -850 nT and 2 minutes before the SMU index peaked at an unusually high value of 720 nT). This MPE occurred at 17:31 MLT. IMF Bz had been strongly negative (-7 nT) for over an hour before the MPE, which, as will be shown in **Figure 14**, occurred while Kuujjuarapik was beneath an eastward electrojet and a downward region 2 field-aligned current. The largest derivative at KJPK, +6.6 nT/s, was in the Bz component as was also the largest derivative observed in the set of stations, which was +17.7 nT/s at INUK.

The MPEs at 01:14, 01:28, 01:42, and 01:54:30 UT on June 17 were located between 20:08 and 20:48 MLT Each was associated with a downward spike in the Bz component, and occurred during an interval when no substorm onsets were identified: the Forsyth et al. (2015) list identified an onset at 00:14 UT, 1 h before the first MPE in the series, and the Forsyth et al. (2015) and Ohtani and Gjerloev (2020) lists identified an onset at 02:58 UT, over an hour after the last MPE in the series. **Figure 13** shows that during these events the SML index increased from -450 to -250 nT, with small SML increases correlated in time with 3 of the 4 MPEs. The SMU index varied from 150 to 300 nT, but with no consistent correlation with the MPEs, and IMF Bz oscillated between negative and positive values with little or no temporal correlation with either SML, SMU, or the MPEs. We also note here that in the European sector P6s pulsations were present between midnight and 01:30 UT. During the first and third MPEs **Figures 15** and **17** show that Kuujjuarapik was in the Harang current system region, and a localized upward field-aligned current region repeatedly appeared and disappeared above or to the south of Kuujjuarapik in synchronization with all four of these MPEs.

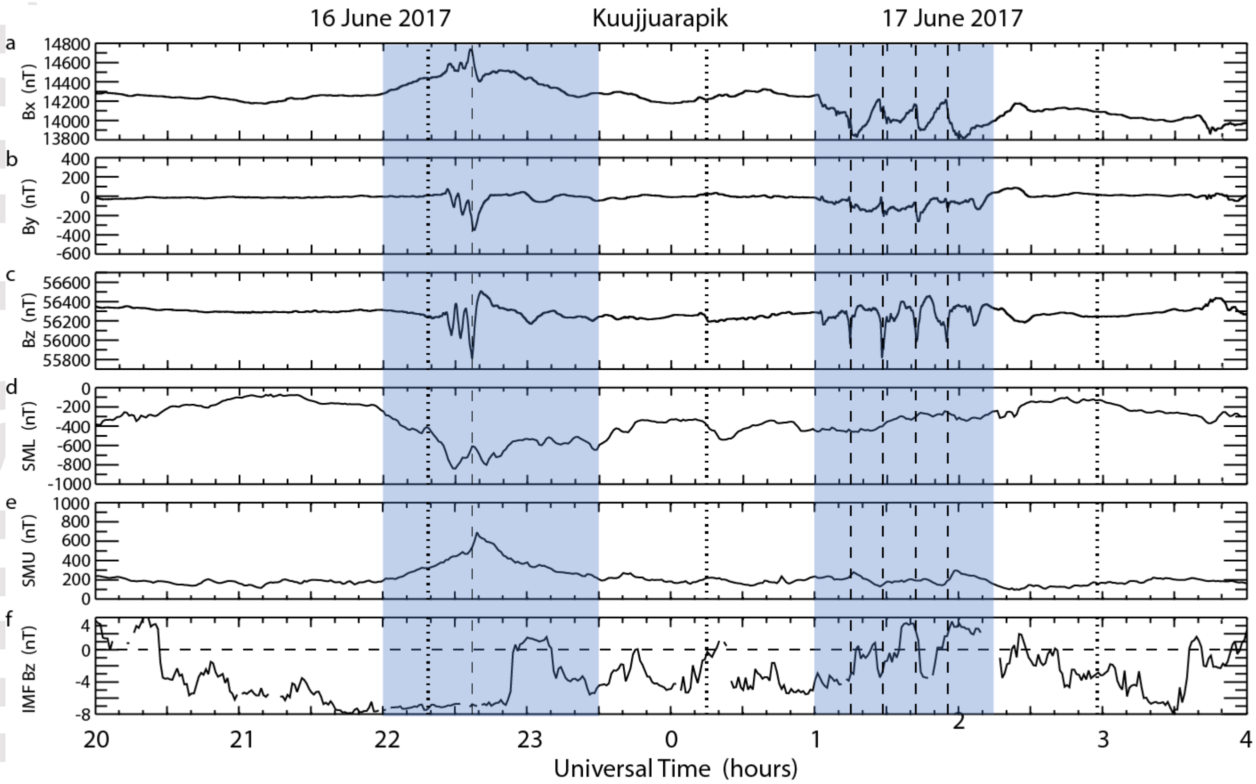

Figure 13. Plot of three components of the magnetic field observed at Kuujjuarapik (panels a-c), the SML and SMU indices (panels d-e), and the Bz GSM component of the IMF (panel f) from 20 UT on 16 June 2017 to 04 UT on 17 June 2017. The times of the MPEs at 22:37 UT June 16 and 01:14, 01:28, 01:42, and 01:54:30 UT on June 17 are indicated by vertical dashed lines, and the times of identified substorm onsets at 22:19 UT, 0:14 UT, and 2:58 UT are indicated by vertical dotted lines.

Table 5 lists the maximum derivatives at seven stations for each of these five MPEs. Their magnitudes during the first event (near 22:37 UT) exceeded 6 nT/s at six of the seven stations, covering a range of 8° in MLAT from CDR to KJPK. In addition, derivatives in the vertical direction (Bz) were the strongest at five of these stations, including the three stations with values exceeding 10 nT/s: at SALU, PUVR, and INUK the derivatives in the north-south (Bx) and east-west (By) directions were of roughly comparable amplitude and often exceeded 6 nT/s. However, the largest derivative was in the vertical direction with |dBz/dt|>10 nT/s. This contrasts to the most common vector orientation for premidnight MPEs (e.g., Viljanen et al., 2001 and Engebretson et al., 2020), with dBx/dt being the strongest and dBy/dt the weakest

The four events between 01:00 and 02:00 UT on 17 June 2017 appeared to be related to a slowly moving intermittent and much more localized "hot spot." Derivatives during the 01:14 UT event exceeded 6 nT/s at three stations: INUK, SNKQ, and KJPK and again had largest amplitude in the vertical direction. However, the derivatives in all three components at SNKQ (located to the west of the line connecting INUK and KJPK) were of comparable size. The amplitude of dBz/dt fell by a factor of 4 (8.4 to 2.1 nT/s) between INUK and PUVR, across a distance of 173 km, and it fell by a factor of 8.3 (12.5 to 1.5 nT/s) between KJPK and RADI, across a distance of 167 km.

The spatial pattern of derivatives during the 01:28 UT event was similar. Derivatives again were largest at INUK, SNKQ, and KJPK and exceeded 10 nT/s at INUK and KJPK, but in this case the *x* component derivative was largest at SNKQ (-13.4 nT/s). Comparison of all three components at these stations as well as at RADI suggests that the center of the MPE at 01:28 UT was slightly south and west of the center during the earlier 01:14 UT event.

The final two events were significantly more intense at INUK, with maximum dBz/dt values of 19.2 and 24.3 nT/s, and strongest in the vertical component at INUK and KJPK, but stronger in both horizontal components at SNKQ. The amplitude of dBz/dt fell between INUK and PUVR by a factor of 8.3 (19.2 to 2.3 nT/s) during the 01:42 UT event, and a factor of 5.6 (24.3 to 4.3 nT/s) during the 01:54 UT event. The last event also showed a slight southwestern progression, with a ~1 min delay between the northern and southern/southwestern stations.

Figures S1 and **S2** in the Supporting Information show plots similar to **Figure 9**, presenting the time series of the MPEs on 16 and 17 June 2017, respectively in all three components at all seven stations. Most notable in **Figure S2** is that the Bx perturbations at INUK and SNKQ were negative for all four MPEs and those at KJPK and RADI became more progressively positive.

Table 5. Maximum derivatives in each component of the magnetic field measured at CDR, SALU, PUVR, INUK, SNKQ, KJPK, and RADI during the MPEs observed near 22:37 UT on 16 June 2017 and at 01:14, 01:28, 01:42, and 01:54 UT on 17 June 2017. In cases when both positive and negative derivatives in a given component were ≥ 6 nT/s both are shown.

Station	Time (HH:MM)	dBx/dt	dBy/dt	dBz/dt
CDR	22:33	-9.2	5.6	-6.2
SALU	22:33	8.8	6.3	-10.4
PUVR	22:36	-6.8	-8.4	13.5
INUK	22:37	-5.0	-8.0	17.7
SNKQ	22:37	-4.4	-6.6	3.4
KJPK	22:37	-3	-4.1	-6.0, 6.6
RADI	22:37	-1.8	-2.2	-1.6
CDR	01:14	0.4	0.6	0.4
SALU	01:14	0.6	-0.7	0.6
PUVR	01:14	-1.1	-1.3	2.1
INUK	01:14	-3.4	-1.0	-8.4,7.6
SNKQ	01:14	-11.9,13.5	-11.9	-14.4
KJPK	01:14	-7.2	-5.5	-10.8,12.5
RADI	01:14	-2.3	-1.9	-1.5
CDR	01:28	0.0	0.4	-0.3
SALU	01:28	1.3	0.7	1.1
PUVR	01:28	2.7	-1.4	3.2
INUK	01:28	-6.8,6.9	-4.0	-15.0,11.2
SNKQ	01:28	-13.4,9.8	-8.8,8.7	-7.1,6.3

KJPK	01:28	-7.0	-8.8	-15.2
RADI	01:28	6.2	-3.3	-3.6
CDR	01:41	-0.6	0.4	0.3
SALU	01:41	-0.7	0.5	-0.8
PUVR	01:41	-3.5	-3.4	2.3
INUK	01:41	-8.0	-6.4	-19.2
SNKQ	01:41	-9.4	-7.3	5.7
KJPK	01:41	-7.9	-4.4	-6.4,6.8
RADI	01:41	-2.4	1.4	-3.5
CDR	01:54	0.7	0.6	0.4
SALU	01:54	2.0	1.1	-2.0
PUVR	01:54	3.6	4.7	-4.3
INUK	01:54	6.1	4.9	24.3
SNKQ	01:54	-11.2	-10	6.3
KJPK	01:54	-4.8	-4.2	6.9
RADI	01:54	-2.9	-1.4	-1.2

Panels a and b of **Figure 14** show SECS maps at 22:34 and 22:37 UT on 16 June 2017. At 22:34 UT a set of four alternating localized upward (red) and downward (blue) vertical current regions extended southward from CDR/SALU to south of RADI, with the upward regions located slightly to the west of the downward regions (see the yellow oval in panel a). By 22:36 UT the strong upward current region between CDR and SALU had weakened (not shown), the weak downward region east of PUVR had strengthened greatly and moved slightly west to near PUVR and INUK. The upward region between INUK and SNKQ also intensified greatly but remained stationary, and the downward current region over RADI had merged into a longitudinally extended region of downward currents but with its northern edge over KJPK remaining nearly stationary. The large-scale eastward electrojet visible to the west and south remained largely over the same locations at both times. The vertical current regions and ionospheric currents above this chain of stations weakened slightly but did not move from 22:36 to 22:38 UT.

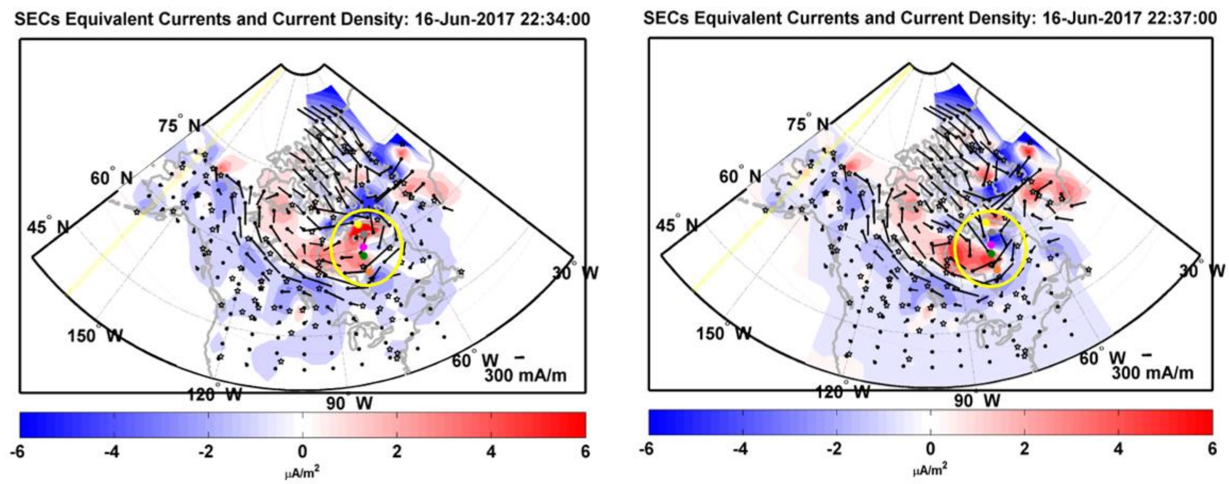

Figure 14. SECS maps of equivalent ionospheric currents and current amplitudes with the same format as **Figure 7**: (a) 22:34 UT, and (b) 22:37 UT, on June 17, 2017.

Panels a-b of **Figure 15** show SECS maps for 01:13 and 01:14 UT on June 17, 2017. Beginning at 01:11 UT, weak and rather stationary localized clockwise vortex in eastern Quebec/Labrador surrounding a downward current gradually intensified through 01:17 UT, but remained nearly stationary through 01:20 UT (not shown). Horizontal currents near SNKQ were near zero through 01:11 UT and vertical currents over SNKQ, KJPK, and RADI were near 0 $\mu A/m^2$ through 01:12 UT, but a weak downward ~1 $\mu A/m^2$ current region appeared over and west of SNKQ at 01:13 UT. An MPE occurred at 01:14 UT when the equivalent current at SNKQ intensified suddenly toward the southwest, but did not strongly resemble a westward electrojet. The equivalent current formed a small vortex surrounding a strong upward current lasting about 1 min. At the same time a strong downward current appeared northward of SNKQ and a strong upward Harang current appeared south of SNKQ and over KJPK and RADI. Both the horizontal and vertical currents remained the same for 3-4 minutes. At 01:17 UT the westward current at SNKQ began to drop, but the direction remained the same and at 01:18 UT the vertical currents moved slightly southward until KJPK was under the downward current, and the westward current at SNKQ decreased considerably (not shown).

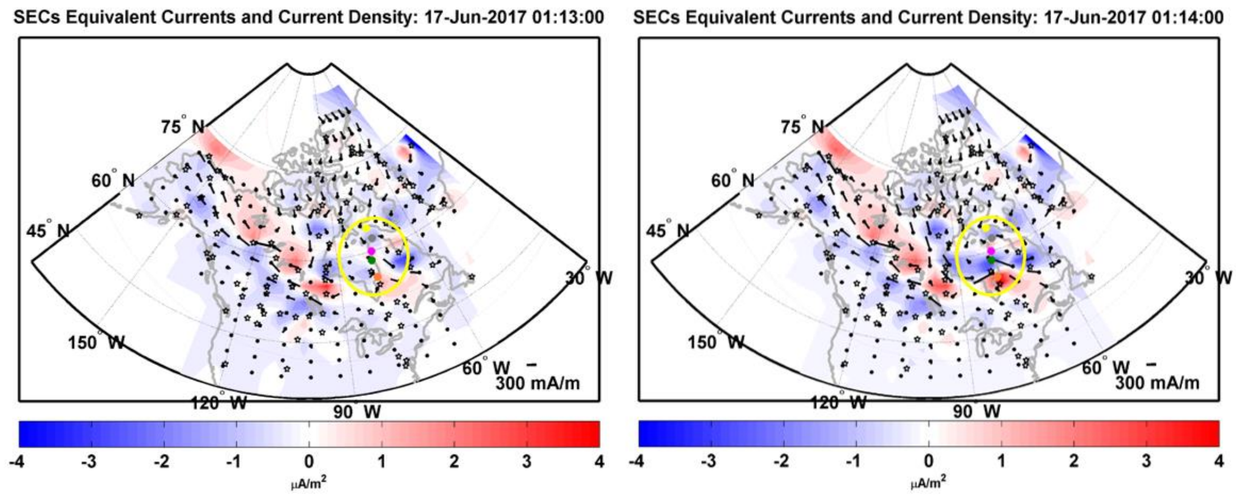

Figure 15. SECS maps of equivalent ionospheric currents and current amplitudes with the same format as **Figure 7**: SECS maps for a) 01:13 and b) 01:14 UT on June 17, 2017. The region where the MPE occurs is circled in yellow.

In **Figure 16** only very weak vertical currents were evident at 01:27 UT over the western edge of Quebec, but strong vertical currents associated with the MPE appeared suddenly at 01:28 UT. The ionospheric current pattern at 01:28 UT resembled a Harang current system in the Hudson Bay region but the region 2 currents were weak south of Hudson Bay and the upward Harang current was not contiguous. We have thus identified this current arrangement as unclear for the electrojets and field aligned currents. During this event a downward current region was centered over INUK and PUVR and an upward region was overhead and to the west of KJPK. After 01:28 UT the vertical currents weakened and moved slightly southward. Prior to the MPE at 01:27 UT there were weak NNW equivalent currents of 128 mA/m near SNKQ (northwest of KJPK) and near RADI (south of KJPK). These were replaced at 01:28 UT by a ~6 times stronger WNW current near SNKQ (678 mA/m) and a weaker NE current of 327 mA/m near RADI, respectively. Again the equivalent current formed a small vortex surrounding a strong upward current at about 01:28 UT lasting about 3 min. Both of these currents weakened again at 01:29 UT to 520 and 202 mA/m, respectively.

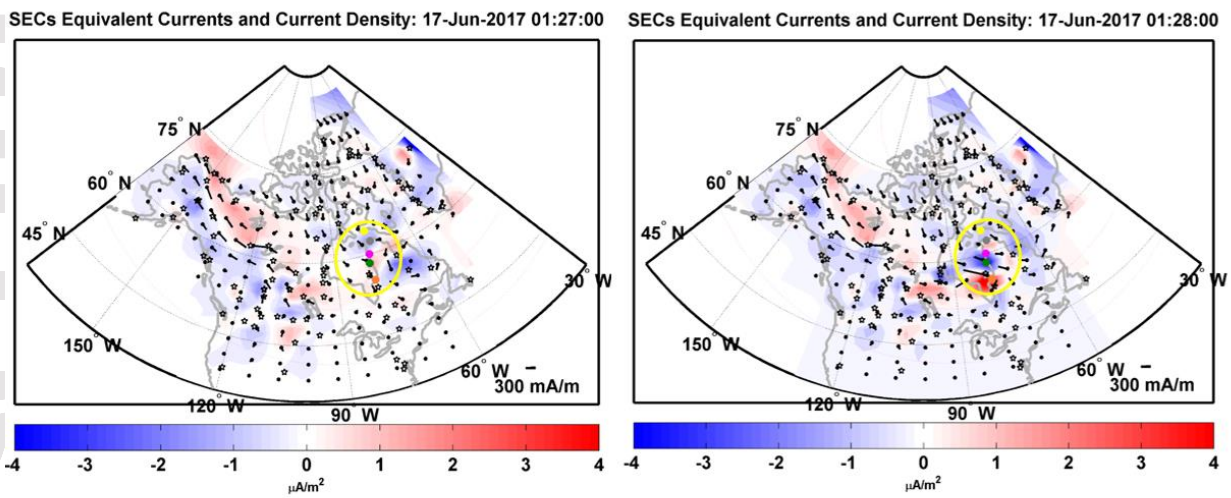

Figure 16. SECS maps of equivalent ionospheric currents and current amplitudes with the same format as **Figure 7**: SECS maps for a) 1:27 and b) 1:28 UT on June 17, 2017.

Approxinately the same current pattern as appeared from 01:27 to 01:28 UT occurred during the third interval from 01:41 to 01:42 UT in **Figure 17**. Just prior to the MPE only very weak vertical currents were evident at 01:41 UT over the western edge of Quebec, but strong vertical currents appeared suddenly at 01:42 UT. A downward region 1 current was centered over INUK and PUVR and an upward current region was overhead and to the west of KJPK. Weak horizontal currents of 180 mA/m near SNKQ at 01:41 UT were replaced at 01:42 UT by a WNW equivalent current that was 3.5 times stronger near SNKQ and a somewhat stronger NE current near RADI of 349 mA/m, respectively. The current pattern in the Hudson Bay region at 01:42 UT is a Harang current system: the westward electrojet extended from the east coast to James Bay and the upward Harang current over KJPK was contiguous. At about 01:42 UT the equivalent current formed a small vortex surrounding a strong upward current lasting about 2 min. These horizontal currents intensified slightly by 01:43 UT, but decreased significantly by 01:44 UT (not shown).

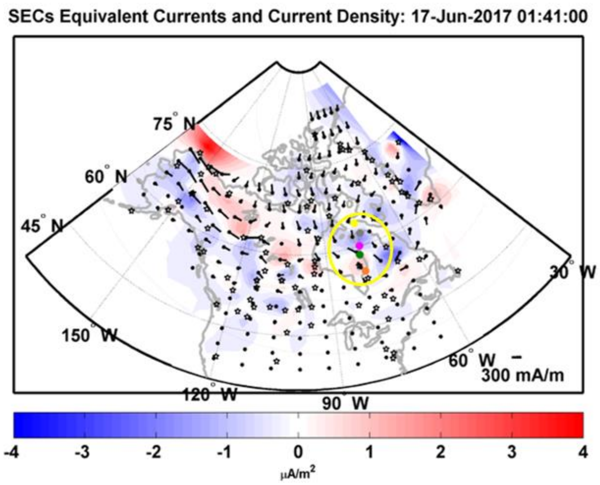

Figure 17. SECS maps of equivalent ionospheric currents and current amplitudes with the same format as **Figure 7**. SECS maps for a) 01:41 and b) 01:42 UT on 17 June 2017.

During the last interval in this series (**Figure 18**), horizontal currents with values of about 600 mA/m extended westward from near INUK from 01:50 to 01:57 UT. The horizontal current extending from northwest of KJPK exhibited a sharp reversal: it was directed toward the northeast from 01:50 to 01:53 UT (not shown) , but dropped to near 0 mA/m at 01:54 UT and pointed WNW with a magnitude of 388 mA/m at 01:55 UT. These changes at KJPK may have been related to the movement of localized downward and upward currents at 01:53 UT that were between SALU and PUVR and between INUK and KJPK, respectively, but had moved toward the southwest by 01:55 UT leaving SNKQ and KJPK in an upward Harang current system and INUK and PUVR in a downward current system.

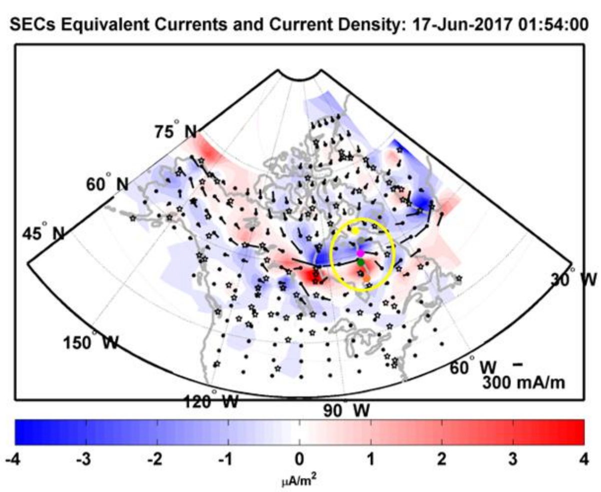

Figure 18. SECS maps of equivalent ionospheric currents and current amplitudes with the same format as **Figure 7**. SECS maps for 1:54 and 1:55 UT on 17 June 2017.

In all the MPEs detailed here an increase in the horizontal currents and current amplitudes was observed. In the next section we will discuss the possible mechanisms by which these MPE have been produced.

6. Discussion

We have presented a number of examples of MPEs and their location within the nightside auroral current system as determined by the SECS technique. A statistical analysis of 279 MPEs at CDR and KJPK indicated that 186 of the events occurred within about 30 minutes of substorm onset and 235 occurred within 60 min of substorm onset, where the substorm onset is defined by the SML index using the Newell and Gjerloev (2011), Forsyth et al. (2015), and Ohtani and Gjerloev (2020) substorm event lists. One caveat to the substorms used in this study has been discussed in Engebretson et al. (2019a), which is that the initiation of a new substorm may be masked by continuous geomagnetic activity during disturbed conditions and the time delays between substorm onsets and MPE events given in this study under these conditions may be overestimates. The remaining 44 MPEs occurred more than 60 min after the most recent onset. More details on the MPEs and their distribution relative to the substorm onset can be found in Engebretson et al. (2021a).

The statistical study of the locations of MPEs at CDR and KJPK relative to overhead current systems presented in **Table 3** showed that in a large majority of cases, both “premidnight” and “postmidnight” and in all three time delay categories after the substorm onset, the MPEs occurred under the WEJ, and a sizeable number of “premidnight” events occurred beneath the upward Harang current system. These patterns suggest that instabilities associated with these regions may be responsible for many of these intense and sudden magnetic perturbations. The “postmidnight” events were found to occur beneath the downward region 1 and upward region 2 current systems, but a significant number were unclear. However, the increasing association of many MPEs with other current systems (both horizontal and vertical) with increasing time delay after substorm onsets suggests the complexity and possible multiplicity of their drivers.

The four case study intervals in section 5 provide a variety of temporal contexts for MPE occurrences. The 7 April 2015 event occurred 7 min after a substorm onset, under non-storm conditions. The 19 April 2015 event occurred 2+ days after a strong (SYM/H ~ -90 nT) geomagnetic storm, and 1 minute after a weak substorm onset or pseudobreakup. The two 23 March 2017 events occurred during the early recovery phase of a weak (SYM/H ~ -45 nT) geomagnetic storm; a weak substorm onset was identified in two of three substorm lists 4 minutes after the first MPE and 13 minutes before the second MPE. The June 16 2017 MPE occurred during the main phase of a weak (SYM/H ~ -40 nT) geomagnetic storm that was related to the passage of a high speed stream and 18 minutes after a substorm onset. The four MPEs early on 17 June 2017 occurred during the early recovery phase of this geomagnetic storm, and no substorm onsets occurred within 1 hour before or after this interval. The IMF Bz component was fully or partly < 0 nT before each MPE.

Each case study showed 8 hours of magnetic field data from one station as well as SML and SMU activity index data and time-shifted IMF Bz component data, and by means of the SECS technique, displayed rapid (1-min) variations in empirically derived ionospheric equivalent currents and current amplitudes that were associated with each MPE. In two of the four cases auroral imager data provided complementary information. In the following paragraphs we summarize the findings of each of these case intervals and suggest possible causal relations between these currents and auroral structures and the MPEs.

The 7 April 2015 MPE event at 02:24 UT was closely associated in time with an isolated substorm onset at 02:17 UT and a subsequent sharp ~-220 nT spike in SML, reaching -274 nT at 02:23 UT before retreating. The IMF Bz component was negative for most of the previous hour, including the last 7 min before MPE occurrence. SECS maps showed that a WEJ grew gradually from a quiet background beginning near 02:15 UT, with a downward current to the north of CDR and an upward current to the south. Both current regions moved northward from 02:19 through 02:23 UT, at which time the upward current region was over CDR and the WEJ peaked at 601 mA/m. The MPE thus could clearly be associated with a short-lived and spatially localized intensification of the WEJ and associated localized upward and downward FACs.

The 19 April 2015 MPE event at 04:10 UT closely followed an isolated substorm onset at 04:09 UT and a rapid ~-200 nT negative spike in SML, reaching -325 nT at 04:13 UT. The IMF Bz was <0 nT for the previous 4 hours, but rotated toward 0 nT during the last 6 min before the MPE. SECS maps showed that the MPE was associated with the rapid intensification and southward movement of a pair of localized downward and upward currents, the appearance of a latitudinally narrow but longitudinally extended WEJ, and the rapid appearance, slower westward motion, and localized twisting of an east-west auroral arc.

The 23 March 2017 MPE at 01:18 UT occurred within a ~40 min interval of nearly constant SML index near -200 nT. It was associated with the sudden appearance of regions of localized upward current (overhead and to the north of INUK) and downward current (to the south of INUK) and of a WNW equivalent current between them. This localized current was again accompanied by a greatly intensified east-west auroral arc. The second MPE at 01:35 UT on this day was more extended in latitude. Only weak downward currents were evident in the region from SALU to INUK until 01:35 UT, along with a pair of moderately strong localized downward and upward currents from INUK through RADI. An intense upward current region appeared suddenly between SALU and INUK at 01:35 UT, while the localized downward current between INUK and KJPK intensified but its location did not change. The occurrence of the MPE was simultaneous with the movement of an intense and wide auroral streamer into the region between SALU and INUK from the northeast.

The 16 June 2017 MPE at 22:37 UT occurred 18 min after a substorm onset (identified in only one of the three substorm lists) and in association with a gradual ~600 nT drop in SML to ~-850 nT and an unusually large SMU peak of 720 nT. Before the MPE, KJPK was located under the northern edge of a large-scale EEJ, and an alternating set of localized upward and downward currents stretched latitudinally across the entire set of stations. The pair of vertical currents between SALU and KJPK both intensified at the time of the MPE, but showed little spatial motion.

As shown in **Figure 13**, only minor variations in the SML index appeared during any of the four MPEs recorded at KJPK between 01:00 and 02:00 UT on 17 June 2017. The most prominent feature of the first three of these (at 01:14, 01:28, and 01:42 UT) was the sudden appearance, within 1 min, of a localized downward current between INUK and SNKQ and a similarly localized upward current to the south, between KJPK and RADI. The MPE at 01:54 UT was more closely related to the rapid southwest movement of a similar pair of localized upward and downward current regions. Unfortunately, no auroral images were available during any of these events.

Engebretson et al. (2019a) has previously reported the approximate radius of MPEs to be about 275 km. The radius estimate was based on the area of the dB/dt at half the peak value from a superposed epoch analysis, and this size is larger than the resolution of the spherical elementary currents. The cases discussed in section 5 had dB/dt values of 6 nT/s up to 24 nT/s. Using the same method applied in Engebretson et al. (2019a), but for each individual event, we determined the approximate radius in the latitudinal direction (i.e., not all the MPEs are circular) of the nine MPEs discussed in section 5. In general, approximately 7 to 10 stations within the region contribute to the determination of the radius. The values ranged from 243 to 444 km with a mean of 304 km, median of 288 km, and standard deviation of 62 km, where the mean is within one standard deviation to the value published in Engebretson et al. (2019a). The last column of **Table 6** displays the determined radius of each MPE. We also note that the area of these MPEs is similar to the area of the auroral enhancements observed in the all sky images shown for 19 April 2015 and 23 March 2017.

Auroral images available for some of the MPE shown here and in prior studies (Engebretson et al., 2019b) resemble ripples and vortices. We suggest here that MPEs are associated with intermittent instabilities that can produce turbulent magnetic field fluctuations within the magnetotail. Probability distribution functions of ΔB and dB/dt discussed in Engebretson et al. (2019a) support this comment. Observations of intermittent magnetic field turbulence within the magnetotail plasma sheet have been previously discussed in Weygand et al. (2005; 2006). Another possibility is a solar wind source or trigger for MPEs. However, given the currently limited spacecraft coverage in both the magnetotail and solar wind, it is difficult to find events in these regions that might correlate in time with any given MPE.

7. Summary and Conclusions

In this study we have used magnetometer and auroral imager observations in eastern Arctic Canada to provide more detailed information about the characteristics and locations of nightime MPEs relative to ionospheric and field-aligned current regions in the auroral zone.

Using a database of 158 MPEs observed at Cape Dorset (75.2° MLAT) and 121 MPEs observed at Kuujuarapik (64.7° MLAT) in Arctic Canada during 2015 and 2017, in combination with SECs maps of equivalent ionospheric and current amplitudes over North America and Greenland, we have identified the types of current systems beneath which these MPEs occurred. Even when separated into "premidnight" and "postmidnight" local time categories and three categories of time delay after the most recent substorm onset (0-30 min, 30-60 min, and > 60 min), most MPEs occurred under a WEJ, and a sizeable number of "premidnight" events occurred beneath the upward Harang current system. "Postmidnight" events were most commonly associated with upward region 2 currents (60%), but another 24% were associated with downward region 1 currents.

These MPE distributions suggest that possibly several types of phenomena associated with WEJ and/or Harang current system may be responsible for many of these sudden and intense magnetic perturbations. However, the percentage of MPEs associated with other current systems (both horizontal and vertical) or for which there was no clear association increased with increasing time delay after substorm onsets. This suggests the complexity and possible multiplicity of their drivers even for premidnight events.

Equivalent ionospheric currents determined by the SECS method have been used in several previous event studies of MPEs located in North America (Ngwira et al., 2018; Engebretson et al., 2019a,b; Nishimura et al., 2020) as well as in Fennoscandia (Huttunen et al,, 2002; Pulkkinen et al., 2003; Apatenkov et al., 2004; Belakhovsky et al., 2019; Dimmock et al., 2019; Apatenkov et al., 2020). This study presented similar SECS maps of both horizontal and vertical currents at a 1 min cadence during four intervals of MPE activity, focusing especially on the chain of stations from CDR to RADI from southern Baffin Island southward along the east coast of Hudson Bay. These intervals provided a variety of temporal contexts for MPE occurrences. The only common factor was that the IMF Bz component was fully or intermittently negative from 1 to 4 hours before each MPE. This Bz direction is consistent with the patterns found in several earlier studies of these events (e.g., Apatenkov et al., 2004; Huttunen et al., 2004; Belakhovsky et al., 2019, Dimmock et al., 2019, 2020; Engebretson et al. 2019a; and most recently in the superposed epoch study of Engebretson et al., 2021b).

Table 6 summarizes the conditions under which the MPEs during these intervals occurred. They differed in the phase of magnetic storms under which they occurred, their temporal relation to substorm onsets, their similarity (or not) to variations in the SML index, their approximate full-width half-max radius, and the characteristics of overhead currents and aurora.

Table 6 : Summary of the Associations of the case study MPEs to geomagnetic storms, substorm onsets, SML variations, and changes in overhead currents. The question mark under the substorm onsets column means the onset time was unclear.

Event	**Storm Phase**	**Substorm Onsets**	**SML Variations**	**Overhead Currents**	**Aurora**	**Max. Derivatives**	**Radius (km)**
1	Non-Storm	7 min prior	-220 nT Spike	Motion and Local Intensification	No Data	6.8 nT/s dBx/dt	307
2	Late Recovery	1 min prior?	-200 nT Spike	Local Intensification	E-W Arc Appears	-9.7 nT/s dBz/dt	444
3A	Early	4 min	< 50 nT	Local	E-W Arc	-29.5 nT/s	269

	Recove ry	after	Increase	Intensificatio n	Intensifie s	dBz/dt	
3B	Early Recove ry	13 min befores	-200 nT Spike	Local Intensificatio n	Streamer from NE.	13.3 nT/s dBz/dt	269
4A	Main Phase	None	+200 nT Increase	Motion and Local Intensificatio n	No Data	17.7 nT/s dBz/dt	251
4B	Early Recove ry	None	450 nT Flat	Local Intensificatio n	No Data	13.5 nT/s dBx/dt	288
4C	Early Recove ry	None	+150 nT increase	Local Intensificatio n	No Data	-15.0 nT/s dBz/dt	352
4D	Early Recove ry	None	+ 50 nT increase	Local Intensificatio n	No Data	-19.2 nT/sdBz/dt	243
4E	Early Recove ry	None	< 50 nT Increase	Motion	No Data	24.3 nT/s dBz/dt	320

The statistical results and case studies in Tables 3 and 6 demonstrate that MPEs are associated with a range of current systems, geomagnetic conditions, auroral structures, and potentially dangerous values of dB/dt over large regions. Furthermore, their scale size stretches over 100s of kms. We reiterate that MPEs are of interest because they can potentially produce GICs that can interfere with technological systems. Further studies are warranted to understand and potentially predict MPEs.

Acknowledgments

This research was also supported by NSF grants AGS-1651263 and AGS-2013648 to Augsburg University, AGS-1654044 and AGS-2013433 to the University of Michigan, AGS-1502700 to JHU/APL, and at UCLA by the MMS project. Martin Connors thanks NSERC for research support and the Canadian Space Agency for support of AUTUMNX. The spherical elementary currents produced by J.M. Weygand were made possible by NASA grants 80NSSC18K1220, 80NSSC18K1227, 80NSSC20K1364, 80NSSC18K0570, and NASA Contract 80GSFC17C0018. The work of Dr. Y. Nishimura was supported by NASA grant 80NSSC18K0657, 80NSSC20K0604 and 80NSSC20K0725, NSF grant AGS-1907698, and AFOSR grant FA9559-16-1-0364. The THEMIS ASIs are supported by Canadian Space Agency. The work by Dr. L.R. Lyons was supported by NSF grant 20191955.

Data Availability Statement

MACCS magnetometer data are available at http://space.augsburg.edu/maccs/requestdatafile.jsp and
AUTUMNX magnetometer data are available in IAGA 2002 ASCII format at http://autumn.athabascau.ca/autumnxquery2.php?year=2015&mon=01&day=01.

SECS maps of North America from 2007 through 2019 are available at a 1-minute cadence at http://vmo.igpp.ucla.edu/data1/SECS/Quicklook/.

THEMIS auroral imager data are available at the website (http://themis.ssl.berkeley.edu).

The SML and SMU indices are available at http://supermag.jhuapl.edu/indices/ , and the SuperMAG substorm database is available online at http://supermag.jhuapl.edu/substorms/. Jesper Gjerloev is SuperMAG Principal Investigator. These SuperMAG products are derived from magnetometer data from INTERMAGNET, Alan Thomson; USGS, Jeffrey J. Love; CARISMA, PI Ian Mann; CANMOS, Geomagnetism Unit of the Geological Survey of Canada; The S-RAMP Database, PI K. Yumoto and Dr. K. Shiokawa; The SPIDR database; AARI, PI Oleg Troshichev; The MACCS program, PI M. Engebretson; GIMA; MEASURE, UCLA IGPP and Florida Institute of Technology; SAMBA, PI Eftyhia Zesta; 210 Chain, PI K. Yumoto; SAMNET, PI Farideh Honary; IMAGE, PI Liisa Juusola; Finnish Meteorological Institute, PI Liisa Juusola; Sodankylä Geophysical Observatory, PI Tero Raita; UiT the Arctic University of Norway, Tromsø Geophysical Observatory, PI Magnar G. Johnsen; GFZ German Research Centre For Geosciences, PI Jürgen Matzka; Institute of Geophysics, Polish Academy of Sciences, PI Anne Neska and Jan Reda; Polar Geophysical Institute, PI Alexander Yahnin and Yarolav Sakharov; Geological Survey of Sweden, PI Gerhard Schwarz; Swedish Institute of Space Physics, PI Masatoshi Yamauchi; AUTUMN, PI Martin Connors; DTU Space, PI Dr. Thom R. Edwards and Anna Willer; PENGUIn; South Pole and McMurdo Magnetometer, PIs Louis J. Lanzerotti and Allan T. Weatherwax; ICESTAR; RAPIDMAG; British Antarctic Survey; McMAC, PI Dr. Peter Chi; BGS, PI Dr. Susan Macmillan; Pushkov Institute of Terrestrial Magnetism, Ionosphere and Radio Wave Propagation (IZMIRAN);; MFGI, PI B. Heilig; Institute of Geophysics, Polish Academy of Sciences, PI Anne Neska and Jan Reda; and University of L'Aquila, PI M. Vellante; BCMT, V. Lesur and A. Chambodut; Data obtained in cooperation with Geoscience Australia, PI Marina Costelloe; AALPIP, co-PIs Bob Clauer and Michael Hartinger; SuperMAG, Data obtained in cooperation with the Australian Bureau of Meteorology, PI Richard Marshall. Finally, we would like to thank Dr. David Boteler for providing magnetometer data from Natural Resources Canada.

References

Amm, O., and A. Viljanen, (1999), Ionospheric disturbance magnetic field continuation from the ground to the ionosphere using spherical elementary currents systems. *Earth, Planets and Space*, *51*(6), 431–440, https://doi.org/10.1186/BF03352247.

Apatenkov, S. V., V.A. Pilipenko, E.I. Gordeev, A. Viljanen, L. Juusola, V.B. Belakhovsky, and V.N. Selivanov, V. N. (2020). Auroral omega bands are a significant cause of large geomagnetically induced currents. *Geophysical Research Letters*, *47*, e2019GL086677, https://doi.org/10.1029/2019GL086677.

Apatenkov, S. V., V. A. Sergeev, R. Pirjola, and A. Viljanen (2004), Evaluation of the geometry of ionospheric current systems related to rapid geomagnetic variations, *Annales Geophysicae, 22*, 63-72, https://doi.org/10.5194/angeo-22-63-2004.

Belakhovsky, V., V. Pilipenko, M. Engebretson, Ya. Sakharov, and V. Selivanov (2019), Impulsive disturbances of the geomagnetic field as a cause of induced currents of electric power lines, *Journal of Space Weather and Space Climate, 9*, A18, https://doi.org/10.1051/swsc/2019015.

Connors, M., I. Schofield, K. Reiter, P.J. Chi, K.M. Rowe, and C.T. Russell, (2016), The AUTUMNX magnetometer meridian chain in Québec, Canada, *Earth, Planets and Space*, *68*, https://doi.org/10.1186/s40623-015-0354-4.

Dimmock, A. P., L. Rosenqvist, J.-O. Hall, A. Viljanen, E. Yordanova, I. Honkonen, Mats André, and E. C. Sjöberg (2019). The GIC and geomagnetic response over Fennoscandia to the 7–8 September 2017 geomagnetic storm. *Space Weather, 17*, 989–1010, https://doi.org/10.1029/2018SW002132.

Dimmock, A. P., D. T. Welling, L. Rosenqvist, C. Forsyth, M. P. Freeman, I. J. Rae, A. Viljanen, E. Vandegriff, R., R. J. Boynton, M. A. Balikhin, and E. Yordanova, Modeling the geomagnetic response to the September 2 2017 space weather event over Fennoscandia using the Space Weather Modeling Framework: studying the impacts of spatial resolution, submitted to Space Weather, 2021, doi:2020SW002683.

Engebretson, M. J., W. J. Hughes, J. L. Alford, E. Zesta, L. J. Cahill, Jr., R. L. Arnoldy, and G. D. Reeves (1995), Magnetometer array for cusp and cleft studies observations of the spatial extent of broadband ULF magnetic pulsations at cusp/cleft latitudes, *Journal of Geophysical Research*, *100*, 19371-19386, https://doi.org/10.1029/95JA00768.

Engebretson, M. J., V.A. Pilipenko, L.Y. Ahmed, J.L. Posch, E. Steinmetz, E.M.B. Moldwin, M.G. Connors, J.M. Weygand, I.R. Mann, D.H. Boteler, C.T. Russell, and A.V. Vorobev, A. V. (2019a). Nighttime magnetic perturbation events observed in Arctic Canada: 1. Survey and statistical analysis. *Journal of Geophysical Research: Space Physics*, *124*, 7442-7458, https://doi.org/10.1029/2019JA026794.

Engebretson, M. J., E.S. Steinmetz, J.L. Posch, V.A. Pilipenko, M.B. Moldwin, M. G., Connors, D.H. Boteler, I.R. Mann, M.D. Hartinger, J.M. Weygand, L.R. Lyons, Y. Nishimura, H.J. Singer, S. Ohtani, C.T. RussellA. Fazakerley, and L.M. Kistler, (2019b). Nighttime magnetic perturbation events observed in Arctic Canada: 2. Multiple-instrument observations. *Journal of Geophysical Research: Space Physics*, *124*, 7459-7476, https://doi.org/10.1029/2019JA026797.

•Engebretson, M.J., K.R. Kirkevold, E.S. Steinmetz, V.A. Pilipenko, M.B. Moldwin, B.A. McCuen, C. R. Clauer, Michael D. Hartinger, Shane Coyle, Hermann Opgenoorth, Audrey Schillings Anna N. Willer, Thom R. Edwards, David H. Boteler, Andy J. Gerrard, Mervyn P. Freeman, Michael C. Rose (2020). Interhemispheric comparisons of large nighttime magnetic perturbation events relevant to GICs. *Journal of Geophysical Research: SpacePhysics*, *125*, e2020JA028128, https://doi.org/10.1029/2020JA028128.

•Engebretson, M. J., V. A. Pilipenko, E. S. Steinmetz, M. B. Moldwin, M. G. Connors, D. H. Boteler, H. J. Singer, H. Opgenoorth, A. Schillings, S. Ohtani, J. Gjerloev, and C. T. Russell (2021a), Nighttime magnetic perturbation events observed in Arctic Canada: 3. Occurrence and amplitude as functions of magnetic latitude, local time, and magnetic disturbances, *Space Weather, 19*, e2020SW002526, https://doi.org/10.1029/2020SW002526.

•Engebretson, M. J., Ahmed, L. Y., Pilipenko, V. A., Steinmetz, E. S., Moldwin, M. B., Connors, M. G., Boteler, D. H., Weygand, J. M., Coyle, S., Ohtani, S., Gjerloev, J., and Russell, C.T. (2021b), Superposed epoch analysis of nighttime magnetic perturbation events observed in Arctic Canada submitted to the *Journal of Geophysical Research: Space Physics* April 19, 2021, https://doi.org/2021JA029465.

•Forsyth, C., I. J. Rae, J. C. Coxon, M. P. Freeman, C. M. Jackman, J. Gjerloev, and A. N. Fazakerley (2015), A new technique for determining Substorm Onsets and Phases from Indices of the Electrojet (SOPHIE), *J. Geophys. Res. Space Physics*, *120*, 10,592–10,606, doi:10.1002/2015JA021343.

•Huttunen, K. E. J., Koskinen, H. E. J., Pulkkinen, T. I., Pulkkinen, A., Palmroth, M., Reeves, E. G. D., & Singer, H. J. (2002). April 2000 magnetic storm: Solar wind driver and magnetospheric response. *Journal of Geophysical Research*, *107*(A12), 1440, https://doi.org/10.1029/2001JA009154.

•Mende, S. B., S.E. Harris, H.U. Frey, V. Angelopoulos, C.T. Russell, E. Donovan, B. Jackel, M. Greffen, and L. M. Peticolas, (2008). The THEMIS array of ground-based observatories for the study of auroral substorms. *Space Science Reviews, 141*, 357. https://doi.org/10.1007/s11214-008-9380-x.

•Nakamura, R., T. Oguti, T. Yamamoto, and S. Kokubun (1993), Equatorward and Poleward Expansion of the Auroras During Auroral Substorms, *J. Geophys. Res.*, **98**, 5743–5759, doi:10.1029/92JA02230.

•Newell, P. T., and J.W. Gjerloev, (2011a), Evaluation of SuperMAG auroral electrojet indices as indicators of substorms and auroral power, *Journal of Geophysical Research*, *116*, A12211, doi:10.1029/2011JA016779.

•Ngwira, C. M., D.G. Sibeck, M.D.V. Silveira, M. Georgiou, J.M. Weygand, Y. Nishimura, and D. Hampton, (2018), A study of intense local d*B*d*t* variations during two geomagnetic storms, *Space Weather*, *16*, 676–693. https://doi.org/10.1029/2018SW001911.

•Nikitina, L., L. Trichtchenko, and D.H. Boteler, (2016), Assessment of extreme values in geomagnetic and geoelectric field variations for Canada. *Space Weather*, *14*, 481–494, https://doi.org/10.1002/2016SW001386.

•Ohtani, S., and J.W. Gjerloev, (2020). Is the substorm current wedge an ensemble of wedgelets?: Revisit to midlatitude positive bays. *Journal of Geophysical Research: Space Physics*, *125*, e2020JA027902. https://doi.org/10.1029/2020JA027902.

•Viljanen, A.(1997), The relation between geomagnetic variations and their time derivatives and implications for estimation of induction risks, *Geophysical Research Letters*, *24,* 631–634, . https://doi.org/10.1029/97GL00538.

•Viljanen, A., H. Nevanlinna, K. Pajunpää, and A. Pulkkinen, A. (2001), Time derivative of the horizontal geomagnetic field as an activity indicator, *Annales Geophysicae, 19,* 1107– 1118. https://doi.org/10.5194/angeo-19-1107-2001.

•Viljanen, A., E.I. Tanskanen, and A. Pulkkinen, (2006), Relation between substorm characteristics and rapid temporal variations of the ground magnetic field. *Annales Geophysicae*, *24*, 725–733 https://doi.org/10.5194/angeo-24-725-2006.

•Viljanen, A., and E. Tanskanen, (2011), Climatology of rapid geomagnetic variations at high latitudes over two solar cycles. *Annales Geophysicae*, *29*, 1783–1792, doi:10.5194/angeo-29-1783-2011

•Weygand, J. M. (2009a). Equivalent Ionospheric Currents (EICs) derived using the Spherical Elementary Currrent Systems (SECS) technique at 10 s Resolution in Geographic Coordinates, UCLA, https://doi.org/10.21978/P8D62B.

•Weygand, J. M. (2009b). Spherical Elementary Current (SEC) Amplitudes derived using the Spherical Elementary Currents Systems (SECS) technique at 10 sec Resolution in Geographic Coordinates, UCLA, https://doi.org/10.21978/P8PP8X.

•Weygand, J. M., O. Amm, and A. Viljanen, V. Angelopoulos, D. Murr, M.J. Engebretson, H. Gleisner, and I. Mann. (2011). Application and validation of the spherical elementary currents systems technique for deriving ionospheric equivalent currents with the North American and Greenland ground magnetometer arrays. *Journal of Geophysical Research*, *116*, A03305. https://doi.org/10.1029/2010JA016177